

# Reconciling fast and slow cooling during planetary formation as recorded in the main group pallasites

M. Murphy Quinlan\*<sup>1</sup>

A. M. Walker<sup>2</sup>

C. J. Davies<sup>1</sup>

\*Email: eememq@leeds.ac.uk

<sup>1</sup>*School of Earth and Environment, University of Leeds, Leeds, UK*

<sup>2</sup>*Department of Earth Sciences, University of Oxford, Oxford, UK*

March 27, 2023

This paper is a non-peer reviewed preprint submitted to EarthArXiv. This manuscript has been submitted to *Earth and Planetary Science Letters* (EPSL) and is currently under review. If accepted, the final version of this manuscript will be available via the 'Peer-reviewed Publication DOI' link.

Both the main text of the manuscript and the supplementary information are included in this document.

# Reconciling fast and slow cooling during planetary formation as recorded in the main group pallasites

M. Murphy Quinlan\*<sup>1</sup>      A. M. Walker<sup>2</sup>      C. J. Davies<sup>1</sup>

\*Email: eememq@leeds.ac.uk

<sup>1</sup>*School of Earth and Environment, University of Leeds, Leeds, UK*

<sup>2</sup>*Department of Earth Sciences, University of Oxford, Oxford, UK*

March 27, 2023

## 1 **Abstract**

2 Pallasite meteorites contain evidence for vastly different cooling timescales: rapid cooling at high temperatures  
3 (K/years) and slow cooling at lower temperatures (K/Myrs). Pallasite olivine also shows a variety of textures  
4 ranging from well-rounded to angular and fragmental, and some samples record chemical zoning. Previous  
5 pallasite formation models have required fortuitous changes to the parent body in order to explain these  
6 contrasting timescales and textures, including late addition of a megaregolith layer, impact excavation, or  
7 parent body break-up and recombination. We investigate the timescales recorded in Main Group Pallasite  
8 meteorites with a coupled multiscale modelling approach, using a 1D model of the parent body and a 3D  
9 model of the metal-olivine mixing region, to see if these large-scale changes to the parent body are necessary.  
10 We find that the contrasting timescales, textural heterogeneity, and preservation of chemical zoning can all  
11 occur within one simple ellipsoidal segment of an intrusion complex, with  $\sim 12\%$  of our randomly generated  
12 models returning favourable pallasite formation conditions (2200 model runs), with small intrusion volumes  
13 ( $< 5 \times 10^6 \text{ m}^3$ ) and colder background mantle temperatures ( $< 1200 \text{ K}$ ) favourable. Large rounded olivine can  
14 be explained by earlier intrusion of metal into a hotter mantle, suggesting possible repeated bombardment of  
15 the parent body. The formation of pallasitic zones within planetesimals may have been a common occurrence  
16 in the early Solar System, as our model shows that favourable pallasite conditions can be accommodated in  
17 a wide range of intrusion morphologies, across a wide range of planetesimal mantle temperatures, without  
18 the need for large-scale changes to the parent body. We suggest that pallasites represent a late stage of  
19 repeated injection of metal into a progressively cooler planetesimal mantle.

# 1 Introduction

Main Group Pallasite meteorites (referred to from here on as “pallasites”), consisting of a mixture of silicate crystals and FeNi alloy, are believed to represent a key time in the early evolution of the solar system as metal differentiated from silicate and planetary cores began to form. However, models differ about the exact details of the process represented by the pallasite meteorites. In particular, pallasites contain evidence for cooling at contrasting timescales: the metal portion records cooling at rates of  $\sim 10^{-6}$ – $10^{-5}$  Kelvin per year below  $\sim 900$  K (Ni diffusion studies; Yang et al., 1997, 2010; Goldstein et al., 2014), while orders of magnitude more rapid cooling ( $\sim 10^0$ – $10^2$  Kelvin per year) has been suggested to explain chemical gradients and heterogeneity in olivine acquired at higher temperatures (Miyamoto, 1997; Tomiyama and Huss, 2006), and the halted textural equilibration post-metal-injection (Walte and Golabek, 2022). The difference between these rates cannot be explained by a simple conductive cooling model of a planetesimal that initially cools rapidly and then slows (Yang et al., 2010).

The macro-scale texture of pallasite olivine across and within samples ranges from well-rounded to fragmental and highly angular (Grossman and Nomenclature Committee of the Meteoritical Society, 2022). The degree of rounding of olivine grains scales with residence time in hot FeNi (Saiki et al., 2003; Walte et al., 2020), and so the range in degree of olivine angularity across pallasite samples adds further constraints on the cooling rate of the intruded metal in contact with said olivine. The heterogeneity of olivine textures may indicate different formation environments for rounded versus angular olivine crystals, with different temperatures, cooling rates and residence times in molten FeNi metal (McKibbin et al., 2019).

Previous models have suggested injection of metal into a planetesimal mantle via a metallic bolide (Tarduno et al., 2012) or ferrovolcanism from the planet’s molten core (Johnson et al., 2020) in order to explain the delivery of molten metal into the parent body mantle. Metal intrusion formation models typically include a qualitative description of large-scale changes to the parent body following metal intrusion to explain the contrasting timescales recorded in pallasite samples, including impact-related excavation to enable rapid cooling of olivine, the late addition of a thick megaregolith blanket to slow cooling at lower temperatures after the olivine cooling rates were recorded, or the break-up and/or re-combination of the parent body (Bryson et al., 2015; Walte et al., 2020; Yang et al., 2010). Walte et al. (2020) suggest the presence of a small fraction (2–15 vol. %) of ‘primary’ metal trapped in the parent body mantle before the intrusion of ‘secondary’ metal from a bolide, either as residual metal from incomplete parent-body differentiation, or delivered by an earlier impact and subsequently texturally equilibrated (Walte and Golabek, 2022), to facilitate rounding and grain-growth of the largest fraction of rounded olivines over millions of years, and to aid later migration of metal melt through the mantle.

52 The observed cooling-rate constraints and textural details have previously been studied in isolation or  
53 included in descriptive formation hypotheses, and have not been integrated into a single quantitative model  
54 to address whether large-scale changes to the parent body or different formation environments are required  
55 to produce the diversity of time scales and textures seen across Main Group Pallasites.

56 We model the rapid thermal evolution of a metal-olivine intrusion within a slowly cooling mantle in  
57 order to test whether we can reproduce the recorded cooling rates and observed olivine textures in pallasite  
58 samples without ad-hoc changes to the parent body. We assume a separation of timescales such that there  
59 is a one-way interaction between slow cooling of the planetesimal and the fast evolution of the intrusion:  
60 the planetesimal mantle temperature sets the initial and boundary conditions of the metallic intrusion, but  
61 this small metallic intrusion does not influence the slow, large-scale cooling of the planetesimal mantle. We  
62 also investigate the effect of the inclusion of a small fraction of metal in the planetesimal mantle, both on  
63 the cooling of the parent body, and on the cooling of later intrusions into the mantle, in order to address  
64 the possibility of a multi-collisional formation with earlier stranded metal in the mantle. We discuss the  
65 existence of other meteorite groups under the umbrella textural term “pallasite” that formed in different  
66 parent bodies, in distinct regions of the Solar System, and what this implies for the planetary building  
67 process.

## 68 2 Numerical model of a metal intrusion

69 Our conceptual approach of coupling the large-scale, long-term cooling of the pallasite parent body, to the  
70 small-scale, rapid cooling of the intrusion region, can be summarised in five steps (labelled with corresponding  
71 numbers in Figure 1):

**Step 1.** We model the 1D temperature evolution of a simple three-layered parent body, using the method and  
73 planetesimal geometry of the best-fitting result of Murphy Quinlan et al. (2021a): a thick-mantled 250  
74 km radius planetesimal with a core radius of 125 km, and an 8 km-thick megaregolith layer that does  
75 not vary in thickness with time. We repeat this body geometry, with the addition of 15 vol. % metal  
76 in the mantle. We also use an example result from Nichols et al. (2021): a thin-mantled 300 km radius  
77 body with a 250 km radius core, and an 8 km-thick blanket of megaregolith that does not vary in  
78 thickness with time.

**Step 2.** We use the output of step 1 (a time series of temperatures and cooling rates along radius) to calculate  
80 a residence depth for the Imilac meteorite in each parent body, based on the metallographic cooling  
81 rates recorded by Ni diffusion between kamacite and taenite (Yang et al., 2010; Bryson et al., 2015).

82 We infer that this cooling rate is recorded after metal injection, once the metal has cooled to the  
83 background mantle temperature of the parent body, and that it captures the large-scale cooling of the  
84 planetesimal mantle. We focus on this one meteorite as an example, but our results are general and  
85 can be applied across the suite of pallasite meteorites.

**Step 3.** We extract temperature profiles along the planetesimal’s radius, centered at the residence depth  
87 calculated in step two, at times earlier than the metal cooling rates were recorded. We interpolate  
88 these temperature profiles so that they can be used at a smaller metre-scale grid size.

**Step 4.** We consider a cube of mantle material with a vertical temperature gradient set by the background  
90 mantle 1D temperature profile from step three.

**Step 5.** We place an ellipsoid with the material properties of mixed metal and olivine in the centre of this  
92 cartesian box, with an elevated temperature relative to the background mantle (above the liquidus of  
93 FeNi metal), and allow it to cool and crystallise while determining the region’s 3D temperature field.

94 Steps 4 and 5 are developed and discussed in more detail below; information regarding the earlier steps can  
95 be found in Murphy Quinlan et al. (2021a). We use the Imilac meteorite due to paleomagnetic measurements  
96 that add an additional constraint regarding core crystallisation timing (Bryson et al., 2015), but our model  
97 set-up and assumptions can also be applied to other Main Group Pallasite samples. An inherent assumption  
98 of our model is that there is a separation of timescales, implying that there is only one-way interaction between  
99 the slowly cooling parent body mantle, and the rapidly cooling intrusion: while the mantle temperature sets  
100 the boundary condition and initial temperature field of the intrusion model, the intrusion does not effect the  
101 large scale cooling of the mantle. We assume instantaneous emplacement of the molten metal and do not  
102 model deformation associated with intrusion. The results of this intrusion model are then compared to the  
103 evidence from pallasite samples for preservation of chemical heterogeneity and rounding of olivines to see  
104 whether the conditions are favourable for reproducing the known pallasite samples in the meteorite record.

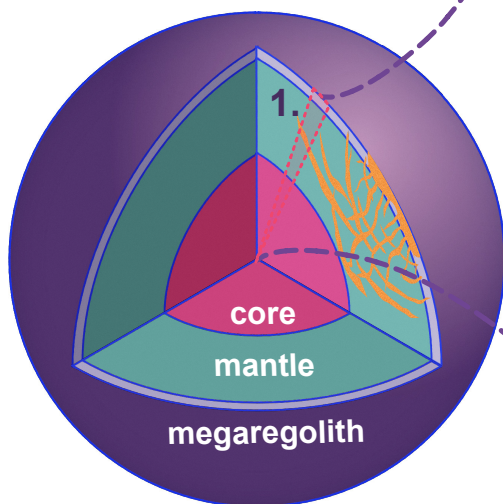
## 105 **2.1 Modelling the intrusion region**

106 Our intrusion model consists of an ellipsoidal region of interconnected solid olivine bridgework (Boesenberg  
107 et al., 2012), the pore space (created by impact-related inter- and intra-granular fracturing) of which has  
108 been infiltrated and saturated by initially molten FeNi metal. This intrusion region is centered in a box  
109 of mantle material (Figure 1; steps 4 and 5) that is below the FeNi solidus. We assume convection of the  
110 metal in this region is inhibited by the low porosity and permeability of the solid olivine bridgework, the  
111 crystallisation of the metal, and the low gravitational acceleration.

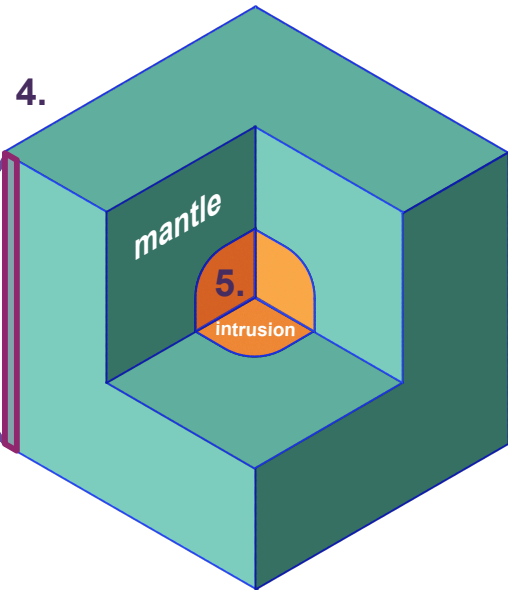
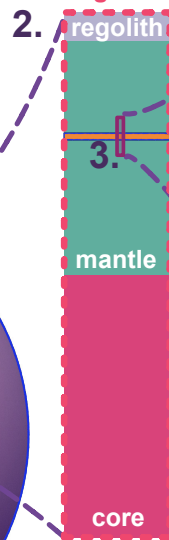
## 1D Planetesimal Model

Murphy Quinlan et al. (2020)

- 1D temperature gradient along radius
- Residence depth of meteorites
- Timing of cooling through  $\sim 800$  K



1D slice  
along radius



## 3D Intrusion Model

This study

- Uses output from planetesimal model as initial conditions
- Cooling rates of metallic intrusion into planetesimal mantle
- Matches fast and slow pallasite cooling rates

Figure 1: Cartoon sketch of model set up; not to scale. 1D temperature, cooling rate, and pallasite residence depth estimation output from the planetesimal model of Murphy Quinlan et al. (2021a) are used as input for a 3D intrusion model; the numbers refer to the modelling method steps laid out in section 2.

112 We consider a cartesian box of mantle material with constant temperature in the horizontal directions  $x$   
 113 and  $y$ , and the vertical coordinate  $z$  aligned with the 1D mantle temperature output from the planetesimal  
 114 model (Figure 1; part three). Assuming a purely conductive system in which convective heat transport and  
 115 internal heat generation are neglected, the temperature  $T$  (K) in this volume satisfies the three-dimensional  
 116 heat conduction equation (Carslaw and Jaeger, 1959):

$$\rho c_p \frac{\partial T}{\partial t} = \frac{\partial}{\partial x} \left( k \frac{\partial T}{\partial x} \right) + \frac{\partial}{\partial y} \left( k \frac{\partial T}{\partial y} \right) + \frac{\partial}{\partial z} \left( k \frac{\partial T}{\partial z} \right) \quad (1)$$

117 where:  $\rho$  is the density of the material ( $\text{kg m}^{-3}$ );  $c_p$  is the specific heat capacity ( $\text{J kg}^{-1} \text{K}^{-1}$ );  $t$  is time  
 118 (s);  $x$ ,  $y$ , and  $z$  are the spatial coordinates (m); and  $k$  is thermal conductivity ( $\text{W m}^{-1} \text{K}^{-1}$ ). We choose  
 119 temperature-independent  $k$ , allowing the Crank-Nicolson scheme to be applied to the problem without the  
 120 complications associated with non-linearity (Carslaw and Jaeger, 1959; Özisik, 1993).

121 We define a uniaxial ellipsoid of volume  $V = \frac{4}{3}\pi a^2 b$ , where  $a$  and  $b$  are radii, which represents the  
 122 intrusion region with a pallasitic mix of silicate and metal. The dimensions of the box ( $X = Y = Z$ ), within  
 123 which this ellipsoid is centered, is set by the diffusion lengthscale for the mantle material: we wish to run  
 124 the model for ten years, and do not want the temperature near the model boundaries to change during that  
 125 time. This allows us to apply a zero-flux condition to the boundaries of the problem.

126 Directly modelling the mixed-phase region of olivine crystals and metal melt would be computationally  
 127 expensive and require detailed knowledge of the geometry of the phase mixture, which we do not know.  
 128 Instead, we take a macroscopic approach to track the cooling and crystallisation of the metal in this area,  
 129 and consider the intrusion region as a single material, using volume-averaged effective thermal properties.  
 130 We adopt the method of Mottaghy and Rath (2006) to model permafrost: we assume a simple saturated two  
 131 component system, where olivine forms a solid interconnected bridgework of crystals, with the pore space  
 132 filled with metal.

133 The fraction of solid and liquid metal is controlled by a temperature-dependent function which should be  
 134 one when the metal is entirely solid ( $T < T_S$ , the FeNi solidus temperature), and zero when the metal is fluid  
 135 ( $T > T_L$ , the FeNi liquidus temperature). In order to account for the latent heat associated with melting or  
 136 crystallisation, we apply the simple fixed-domain apparent heat capacity method (Figure S1) which correlates  
 137 the heat capacity of the phase-changing material with the slope of the enthalpy-temperature curve (Zeneli  
 138 et al., 2021, further details in supplementary materials).

139 The material properties outside the intrusion region have constant values that match that of olivine,  
 140 or a mixture of olivine and 15 vol. % metal; however, phase change processes are not considered for the  
 141 metal in this region. Sudden jumps and step functions in the spatially-varying diffusivity can introduce

142 instabilities especially if these material properties boundaries intersect with the model boundary, so we  
143 surround our intrusion region with mantle material and ensure spatially-constant material properties at the  
144 model boundaries.

145 We apply the semi-implicit Crank-Nicolson scheme (Crank and Nicolson, 1947) with zero-flux boundary  
146 conditions to the heat equation in 1D. Forward difference is used for the time derivative of  $T$ , but the spatial  
147 derivative is evaluated at the time step  $t + \Delta t/2$  instead of at  $t$ , taking the arithmetic mean between the  
148 time step  $t$  and  $t + \Delta t$ . We also discretise  $\kappa$  with respect to distance using finite differences (Langtangen  
149 and Linge, 2017).

150 In order to extend this scheme to three dimensions, we apply the Fractional Step Method (Cen et al.,  
151 2016; Yanenko, 1971), which evaluates the heat equation in one-third time step increments along each of the  
152 spatial dimensions.

153 We bench-marked our numerical model against an analytical solution from Carslaw and Jaeger (1959),  
154 and found that the maximum relative defect between the numerical and analytical models dropped to below  
155 1 % within 150 seconds (Figure S2). We also investigated the effect of spatial resolution on our results to  
156 ensure we chose a sufficiently small spatial step size (Figure S3). Extended methods and full derivations can  
157 be found in the supplementary information.

### 158 **3 Quantitative constraints on the cooling of pallasite meteorites**

159 The results of the model at different times are analysed and compared to the meteorite record. We address  
160 two key criteria: the potential for rounding of olivine grains, and the preservation of primary igneous  
161 zoning. Each intrusion model output is scored based on whether it was consistent with observations from  
162 the meteorite record with respect to these criteria; models with a score of two reproduce both results.

#### 163 **3.1 Textural heterogeneity**

164 According to the Meteoritical Bulletin Database (Grossman and Nomenclature Committee of the Meteoritical  
165 Society, 2022) and the textural descriptions compiled by McKibbin et al. (2019), pallasite meteorite samples  
166 described as having predominantly “rounded” olivine grains constitute 36 % by mass of the Pallasite Main  
167 Group (PMG) meteorite record, while samples with predominantly “angular” olivine constitute 32 % by mass  
168 of the PMG meteorite record (Figure S4). The remaining pallasites show a mix of olivine morphologies, with  
169 both angular and rounded grains present within single samples.

170 Small olivine grains of diameter 300  $\mu\text{m}$  could be rounded within approximately ten years in Fe-Ni-S  
171 at temperatures at or above  $\sim 1573$  K, or within approximately three months at  $\sim 1623$  K (Walte et al.,



172 2020; Saiki et al., 2003). Larger olivines could also be rounded on geologically short timescales at higher  
173 temperatures, or with protracted cooling, or in the presence of sulfide-rich metal melt. However, Walte  
174 et al. (2020) and Walte and Golabek (2022) suggest large rounded olivines predate the pallasite-forming  
175 metal-olivine mixing event and so do not need to be explained in the intrusion process; they are rounded  
176 by a small fraction of metal (2–15 vol. %) retained in the mantle from incomplete differentiation and core  
177 formation, or stranded after partial re-equilibration from an earlier metallic impact. We address this by  
178 increasing the diffusivity of the parent body mantle for a selection of runs to approximate 15 vol. % metal  
179 trapped in the mantle, and track the cooling history at the depth of pallasite residence to see if large-scale  
180 rounding can be achieved prior to secondary metal intrusion.

181 To produce a pallasite sample with a dominantly rounded olivine texture (including the largest size  
182 fraction of olivine, which requires long timescales to round,  $> \text{Myr}$ ), the starting olivine must already be  
183 rounded, and then any small fragments of olivine fractured during the intrusion of metal must be sufficiently  
184 heated for long enough to round post-intrusion. To produce pallasite samples with a dominantly angular  
185 texture, the original pre-intrusion olivine must either be euhedral or “angular”, or if rounded, must be  
186 extensively fractured during metal intrusion. Then, the intrusion region must cool quickly enough to not  
187 modify their angularity.

188 To produce a mixed-type pallasite with both rounded and angular olivine grains, the original olivine  
189 texture could be rounded, with then some fracturing on metal intrusion and subsequent rapid cooling for  
190 preservation of this angularity; or, the original texture could be angular or euhedral with rounding of smaller  
191 grains due to prolonged contact with hot metal post-intrusion. Mixed-type pallasites can also be produced  
192 by pieces of angular or rounded olivine being broken off the bridgework and entrained in the metal melt,  
193 and carried to regions with olivine of a different morphology, followed by rapid cooling which preserved the  
194 textural heterogeneity.

195 While we accept that the meteorite record almost certainly does not accurately and representatively  
196 sample the pallasite formation region of the pallasite parent body, it provides some suggestion of the  
197 proportion of the intrusion region that should produce rounded or angular olivines. We define a volumetric  
198 fraction of the total PMG record expected to have a rounded, angular or mixed olivine texture, by assigning  
199 a dominant texture to each sample in the database, then dividing the recorded sample mass by the average  
200 pallasite density (Grossman and Nomenclature Committee of the Meteoritical Society, 2022; Britt and  
201 Consolmagno, 2003, see supplementary information). We take the dominantly rounded fraction of the  
202 pallasite meteorite record as the minimum required volume proportion of the intrusion within which rounding  
203 occurs, and take the angular fraction of the record as the minimum required volume within which angularity  
204 is preserved. This provides upper and lower bounds on what volume of the intrusion should produce rounded

205 olivine grains; the uncertainty between these upper and lower bounds allows for production and preservation  
206 of mixed-type pallasites.

207 Based on experimental results from Walte et al. (2020), to round small olivine grains we require a point  
208 within the intrusion region to be at or above 1623 K at three months after the start of the model run, or  
209 at or above 1573 K at ten years after the start of the model run. For a model to produce the textures  
210 observed in the pallasite meteorite record, at least 36 % by volume of the intrusion region must experience  
211 a temperature evolution conducive to rounding the smallest olivine grains, and at least 32 % by volume  
212 must cool quickly enough to preserve angular and fragmental olivine. We investigate the sensitivity of the  
213 model to these requirements by both varying the temperature cut-offs by  $\pm 10\%$  and by varying the timing  
214 of the measurement, and find that the earliest requirement ( $T \geq 1623$  K at three months) is the most  
215 sensitive both to changing the time or temperature of this requirement (see Figure S5). As the temperature  
216 constraints are derived from experimental results extrapolated multiple orders of magnitude beyond the  
217 original experimental design (i.e. from hours and seconds to months and years), and the texture estimates  
218 are based on the gross statistical properties of the incomplete meteorite record, incorporating an estimate of  
219 error would imply an unrealistic level of precision.

### 220 **3.2 Chemical heterogeneity**

221 Pallasite olivines display heterogeneous core and rim compositions (Hsu, 2003), with potential oscillatory  
222 zoning in Cr, Al and V recorded in the Imilac meteorite (Chernonozhkin et al., 2021). Preservation of original  
223 igneous compositions is varied, with solid-state diffusive modification of different elements on different scales  
224 recorded across samples (Hsu, 2003). In general, Ca zoning (either diffusion profiles or original heterogeneity)  
225 is pervasive in pallasite olivine and has not been completely homogenised (Hsu, 2003).

226 In an olivine grain of diameter 300–500  $\mu\text{m}$ , Ca will be completely homogenised within four years at  
227  $\sim 1573$  K and within 8 years at  $\sim 1373$  K (Hsu, 2003; Jurewicz and Watson, 1988). This means that to  
228 preserve the Ca heterogeneity in pallasite olivine, including in the smallest size fraction, the majority of  
229 pallasite samples had to cool rapidly enough to prevent this erasure.

230 Based on diffusion studies of Hsu (2003) and Jurewicz and Watson (1988), to preserve zoning we require  
231 that a point within the intrusion region cools below 1573 K within four years, and below 1373 K within eight  
232 years. In order to reproduce the “ubiquitous” preservation of Ca zoning observed in the pallasite meteorite  
233 record Hsu (2003), we require that  $> 95$  % by volume of the intrusion region cools rapidly enough to preserve  
234 Ca zoning. We also set a more lenient requirement of  $> 50$  % by volume to allow for variations in degree of  
235 diffusional modification, to test if this changes the overall trend of results. We use this lower cut-off value of

236  $> 50\%$  for our example case (Fig. 2) to better illustrate our point-by-point filtering approach, but use the  
 237 stricter  $> 95\%$  cut-off when looking at the overall suite of models, and unless otherwise specified refer to  
 238 this as the zoning requirement. As with the rounding criteria, we allowed the temperature requirements to  
 239 vary by  $\pm 10\%$ , and investigated the sensitivity of the model to the times these filters were applied (Figure  
 240 S5).

### 241 3.3 Filtering model output

242 We analyse each model run’s 3D temperature array at three months, four years, eight years, and ten years  
 243 and find the volume of the intrusion region that meets each of the following logical criteria:

$$\begin{aligned}
 R &:= (T_{3\text{mnths}} \geq 1623 \text{ K}) \vee (T_{10\text{yrs}} \geq 1573 \text{ K}), \\
 Z &:= (T_{4\text{yrs}} \leq 1573 \text{ K}) \wedge (T_{8\text{yrs}} \leq 1373 \text{ K}),
 \end{aligned}
 \tag{2}$$

244 where  $R$  represents potential rounding, and  $Z$  denotes potential zoning. Based on the meteorite record  
 245 (Grossman and Nomenclature Committee of the Meteoritical Society, 2022; see supplementary information)  
 246 we assign a score to the model output:

- 247 • If between 36–67 vol.% of the intrusion will round olivine crystals, and  $> 50\%$  or  $> 95\%$   
 248 (depending on the suite of models) will preserve Ca heterogeneity, the output receives a score of two.
- 249 • If the intrusion region meets only one of these criteria, the output receives a score of one.
- 250 • If neither constraint is met, the output receives a null score.

251 We use this simple scoring criteria instead of alternative measures of goodness-of-fit as we are primarily  
 252 interested in whether any models can match these criteria, as opposed to investigating in detail what region  
 253 of parameter space best reproduces certain results. This can be addressed in future work, as the Euclidean  
 254 norm or a similar measurement can be easily incorporated into our framework. We also test the sensitivity  
 255 of the overall score to changing the rounding and zoning criteria. We find that for a spatial step  $\Delta x < 4$  m,  
 256 the result is not impacted by the spatial resolution of the model (Figure S3).

## 257 4 Cooling of a metal intrusion

258 Using the best-fitting model of Murphy Quinlan et al. (2021a), we initially modelled the temperature  
 259 evolution of the mantle of a 250 km radius planetesimal and calculated the residence depth of the Imilac  
 260 pallasite meteorite based on Ni-diffusion cooling rates estimated from its metal portion (Figure 2a; Murphy Quinlan

261 et al., 2021a; Yang et al., 2010; Bryson et al., 2015). The vertical temperature gradient through the mantle at  
262 an earlier time (selected at random, Figure 2b) was then used as the initial condition for the metal intrusion  
263 model (Figure 2c and d). The parameters used for this model are given in table 1.

264 Each node within the intrusion region was filtered as described in section 3.3, and the volume percentage  
265 of the intrusion meeting the rounding requirements and zoning requirements were calculated independently  
266 (Figure 3). Approximately 67 % of the intrusion region cools quickly enough to preserve calcium zoning in  
267 olivine (Figure 3 a), passing the requirement of  $> 50$  % by volume of the intrusion region meeting the zoning  
268 criterion. The rounding requirement is also met by just under 67 % of nodes in the intrusion region, passing  
269 the requirement of between 36–67 % by volume of the region meeting this criterion. The model receives a  
270 score of two, indicating that it meets both requirements.

271 This result demonstrates that an ellipsoidal intrusion of molten metal into a porous olivine planetesimal  
272 mantle can reproduce the necessary thermal evolution pathways both to facilitate the rounding of small  
273 olivine grains, and to allow the preservation of Ca zoning. Within the intrusion region, mean cooling rates  
274 of  $\sim 10$ – $150$  K/Myr are reached, agreeing with the elevated cooling rates suggested by Miyamoto (1997) to  
275 explain olivine diffusion profiles (Figure 3 c). This model also agrees with recorded metal cooling rates due  
276 to the initial and boundary conditions; once the intrusion cools to the background mantle temperature (15 –  
277 50 years by conductive cooling, depending on size of the intrusion), it will continue to cool at the same rate  
278 as the planetesimal mantle, and will cool through the required temperature window at the rate predicted by  
279 metal cooling rates (Bryson et al., 2015; Yang et al., 2010; Murphy Quinlan et al., 2021a).

Parameter	Symbol	Unit	Range/Value	Example model run	References/Notes
<b>Initial conditions</b>					
Intrusion radii	$r_x, r_y, r_z$	m	10–150	72, 72, 92	
Mean radius	$\bar{r}$	m	11–147	79	
Unique/non-unique axes	$b/a$		0.07–15.0	1.28	
Metal fraction (intrusion)	$\phi_m$	vol. fraction	0.05–0.55	0.32	Met. Bull. Database
Trapped metal (in mantle)		vol. fraction	0–0.2	0	Walte et al. (2020)
Background mantle temp. (top)	$T_t$	K	250–1600	847	Murphy Quinlan et al. (2021a)
Background mantle temp. (bottom)	$T_b$	K	265–1665	851	Murphy Quinlan et al. (2021a)
Initial intrusion temp.	$T_i$	K	1600–1900	1660	Assumed above liquidus due to impact heating
<b>Material properties</b>					
<b>Metal</b>					
Density	$\rho_m$	kg m <sup>-3</sup>	7020–7500	7260	Scheinberg et al. (2016)
Conductivity	$k_m$	W m <sup>-1</sup> K <sup>-1</sup>	30–40	35	Scheinberg et al. (2016); Touloukian et al. (1971)
Heat capacity	$c_m$	J kg <sup>-1</sup> K <sup>-1</sup>	820–850	835	Desai (1986)
Diffusivity	$\kappa_m$	m <sup>2</sup> s <sup>-1</sup>	$k_m/(\rho_m c_m)$		
Latent heat of crystallisation	$L$	J kg <sup>-1</sup>	1.33E05 – 2.7E+05	2.56E+05	Scheinberg et al 2016
Liquidus temperature	$T_L$	K	1570–1810	1600	Ehlers (1972)
Solidus temperature	$T_S$	K	1260–1790	1260	Ehlers (1972)
<b>Olivine</b>					
Density	$\rho_{ol}$	kg m <sup>-3</sup>	3320–3360	3341	Su et al. (2018)
Conductivity	$k_{ol}$	W m <sup>-1</sup> K <sup>-1</sup>	2.5–3.4	3	Murphy Quinlan et al. (2021a); Bryson et al. (2015)
Heat capacity	$c_{ol}$	J kg <sup>-1</sup> K <sup>-1</sup>	810–830	819	Su et al. (2018)
Diffusivity	$\kappa_{ol}$	m <sup>2</sup> s <sup>-1</sup>	$k_{ol}/(\rho_{ol} c_{ol})$		
<b>Numerical details</b>					
Time step	$\Delta t$	s	2.63E06	2.63E06	Approx. 1 month
Spatial step	$\Delta x, \Delta y, \Delta z$	m	2	2	Calculated from $L, N$
Box size	$L_x, L_y, L_z$	m	200–800	400	
Number of nodes	$N_x, N_y, N_z$		101– 401	201	$L$ and $N$ balanced to give $\Delta x, y, z = 2$ m
Total iterations			10– 241	121	
Boundary conditions	$\mathbf{b}^n, \mathbf{b}^{n+1}$		Neumann, Dirichlet	Zero flux (Neumann)	
<b>Outputs</b>					
Actual intrusion volume	$V$	m <sup>3</sup>	4.90E03– 1.38E07	1.998E06	
Percentage zoning preserved	$Z$ %	%	0 – 100	67.2	
Percentage rounded	$R$ %	%	0 – 100	66.7	

Table 1: Ranges of parameter values for 2200 model runs, including example model run illustrated in Figures 2 and 3. Ranges given do not include parameter variation for sensitivity testing and benchmarking (see supplementary material for further information).

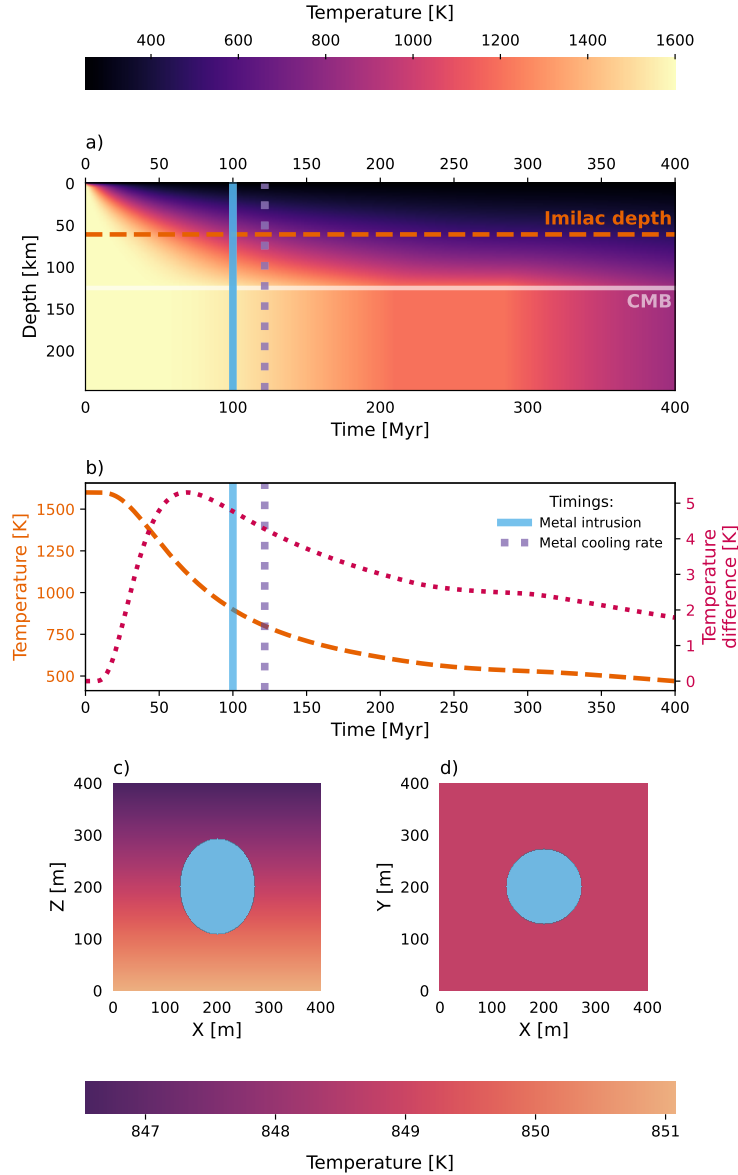


Figure 2: Initial conditions for model run. (a) The 1D temperature evolution for a 250 km radius planetesimal with a 125 km radius core and an 8 km thick porous megaregolith layer (Murphy Quinlan et al., 2021a,b). The core-mantle boundary (CMB) and residence depth of the Imilac pallasite meteorite (61 km, from metal cooling rates; Murphy Quinlan et al., 2021a) are labelled. (b) Temperature profile at this 61 km depth, and temperature difference across a 400 m slice of mantle centred at this depth. These outputs provide the initial and boundary conditions for the intrusion model. The blue vertical line shows the time of intrusion of metal into the mantle (chosen), while the purple dashed line shows the time metallographic cooling was recorded in the pallasite sample (measured). (c & d) Initial conditions for the intrusion model: two 2D slices through the 3D ellipsoid geometry (prolate ellipsoid). Z lies along the planetesimal radius, and shows the vertical temperature gradient, while X and Y have constant temperature. The blue ellipsoid represents the intrusion region, with a temperature of 1790 K.

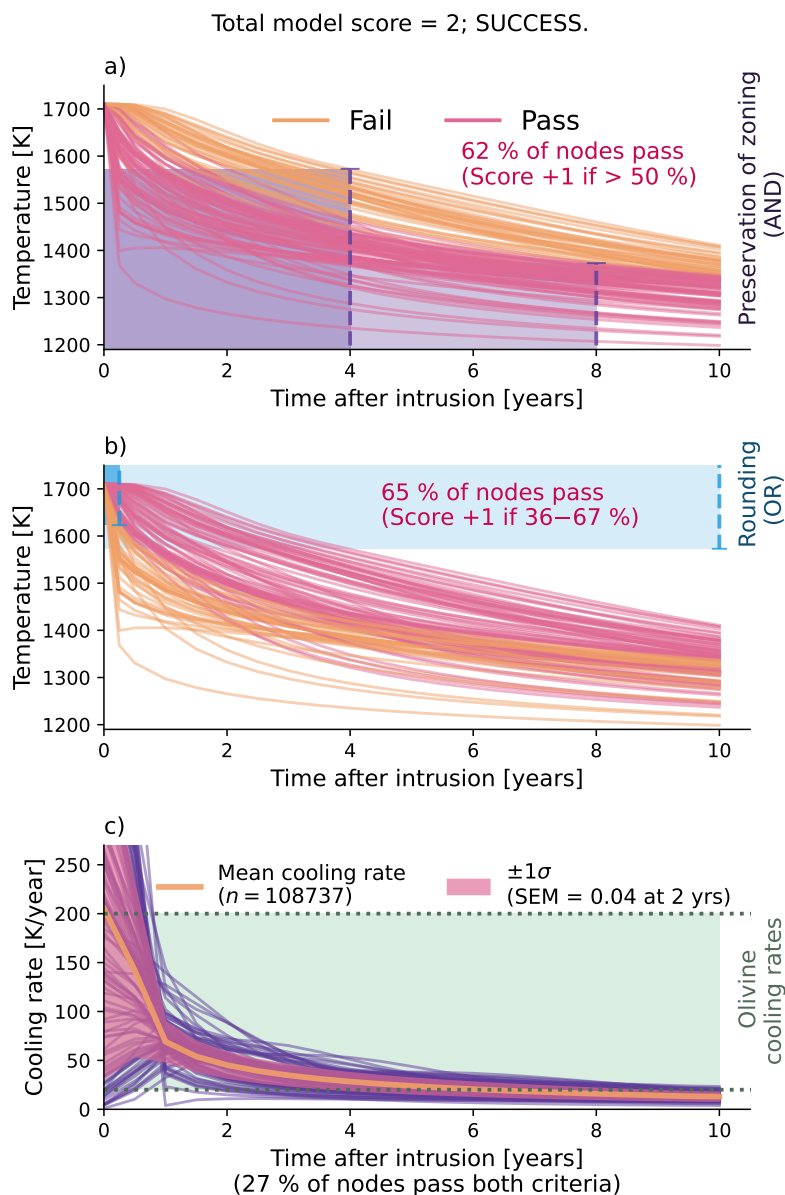


Figure 3: Results and output for a single model run with initial conditions in Figure 2. Each line is a temperature or cooling rate time-series for a volume element within the intrusion described in Figure 2 (e.g. within the blue ellipsoid). Each model is initially assigned a score of zero. Panel (a) shows a sample of nodes (200) within the intrusion filtered according to whether olivine zoning would be preserved at that location. If the model “passes” the zoning preservation criteria ( $> 50\%$  of points will preserve zoning, as is true in this example with  $67.2\%$  passing), one is added to the model’s score. Panel (b) shows the same nodes filtered according to whether olivine grains will be rounded at that location. If the model “passes” the olivine rounding criteria ( $36\text{--}67\%$  of points will round olivine, as is true in this example with  $66.7\%$  of nodes passing), one is added to the model’s score. A score of two is deemed “successful”. The full array of nodes within the intrusion area is used to calculate these percentages (108,737 in this example). Panel (c) shows the cooling rates for the same selection of nodes. The mean cooling rate and standard deviation were calculated with all nodes in the intrusion ellipsoid (108,737). The green shaded region highlights the range of cooling rates suggested by Miyamoto (1997) to explain pallasite olivine zoning.

## 5 Exploring the parameter space

In order to explore how commonly pallasite formation models can yield conditions that preserve the disparate cooling rates, the model procedure was repeated for different intrusion times in the 250 km radius planetesimal (300 models), and for a 300 km radius planetesimal with a 250 km radius core, and an 8 km megaregolith layer (300 models, reproducing a case from Nichols et al., 2021) with randomised intrusion geometry. Randomised initial mantle temperatures were also chosen to approximate different parent body geometries and a range of different intrusion depths (600 models). The summarised results of these 1200 model runs are shown in Figure 4, and ranges within which parameters were varied in table 1. We also ran a suite of 1000 models with varying material properties including density, heat capacity, and crystallisation temperature in addition to randomly selected mantle temperatures and intrusion geometry, which allowed us to approximate the effect of adding a small percentage of trapped metal to the mantle or changing the composition of the intruding metal, as well as testing the model’s sensitivity to these parameters.

Neither initial intrusion temperature (Figure 4, third column) nor metal fraction (by volume, Figure 4, fourth column) strongly control whether the intrusion region will match both constraints. Intrusion volume is a strongly controlling parameter (Figure 4, first column), with the majority of models with a volume greater than  $5 \times 10^6 \text{ m}^3$  meeting neither constraint. While background mantle temperature displays a weak negative relationship with the overall model score, it is strongly negatively correlated with zoning preservation, and moderately positively correlated with rounding potential (Figure S6). Cooler mantle background temperatures (Figure 4, second column) result in higher mean cooling rates and favour meeting both constraints (Figure 4n). These trends hold true not only for model results that use mantle temperature inputs from the planetesimal model, but also for the randomised input parameters that cover a larger parameter space, when material properties are varied randomly, and in the more specific sensitivity tests (Table S1, Figures S7, S8, S9).

Varying the trapped metal content in the mantle or the mantle diffusivity does not systematically change the mean intrusion temperature after ten years, the zoning preserved or the rounding expected (Figure S10), with no significant correlation found between either olivine or metal material properties and model results (Figure S11).

Based on the mean temperature of the intrusion through time, we calculated the mean cooling rate and average temperature of the intrusion between three months and ten years; this allows for an approximate overview of the cooling rate over the model run time, excluding the extremely rapid cooling on initiation of the model. Figure 5 highlights the temperatures and cooling rates relevant to rapid pallasite olivine cooling suggested by Miyamoto (1997); sufficiently high cooling rates are reached in the first few years of cooling.



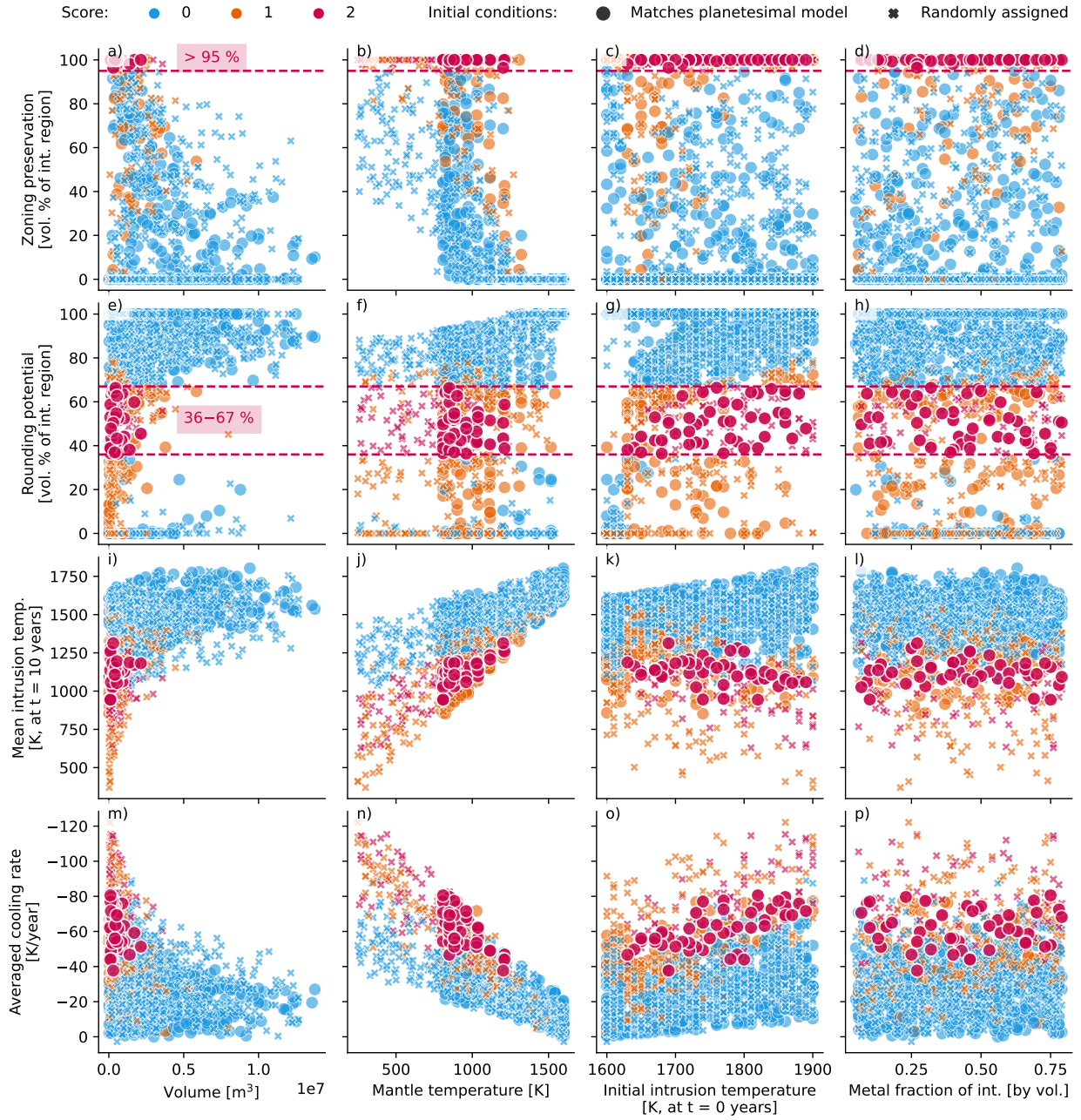


Figure 4: Summary of results for 1000 model runs. Colour denotes score: 0 means neither constraint was matched, 1 means one constraint was matched, and 2 means both constraints were matched. Marker shape describes the initial temperature conditions: either output from a planetesimal model, or randomly assigned. Parameters were not varied in isolation. Large pink circles match both constraints and used input from a planetesimal model.

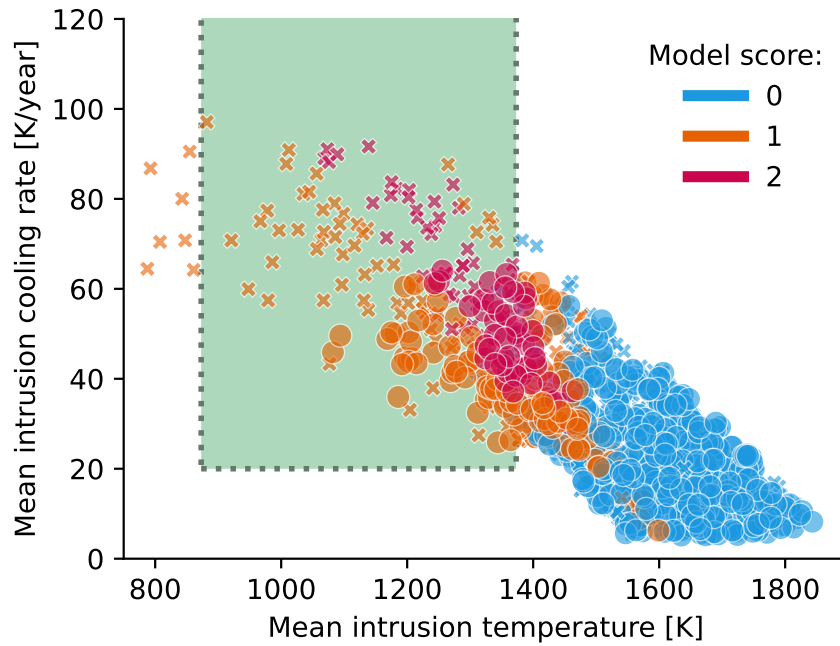


Figure 5: Mean intrusion temperatures and cooling rates over the model run time (from 3 months to 10 years) for the intrusion region for 1200 model runs. The shaded region highlights the cooling rates and temperatures suggested by Miyamoto (1997), estimated from olivine diffusion profiles (Hsu, 2003). Model results that fall within this region reproduce the required rapid cooling in the relevant temperature window. Colour denotes score: 0 means neither constraint was matched, 1 means one constraint was matched, and 2 means both constraints were matched. Marker shape describes the initial temperature conditions: either output from a planetesimal model, or randomly assigned.

312 This suggests that both short-term, rapid cooling of olivine in molten metal, followed by much slower cooling  
313 of the FeNi metal, are explained by the intrusion of hot metal into a warm mantle.

## 314 6 Discussion

315 A simple model of a metallic intrusion into the mantle of a planetesimal reproduces the gross statistical  
316 properties of olivine texture and diffusive modification observed in pallasite meteorites, and replicates the  
317 contrasting slow metal and rapid olivine cooling rates estimated from various elemental diffusion profiles.  
318 This model reproduces these results without the need for impact-exhumation or parent body break-up to  
319 explain rapid olivine cooling rates, or the addition of a late thick megaregolith layer to explain slow cooling,  
320 as have been invoked by previous models (Yang et al., 2010; Bryson et al., 2015; Walte et al., 2020; Walte  
321 and Golabek, 2022).

322 Walte and Golabek (2022) list the observational constraints from pallasite samples that formation models  
323 much match, comprising: remnant magnetisation, a warm mantle prior to pallasite formation, rapid cooling  
324 at high temperatures ( $>1200$  K), slow cooling at lower temperatures (1000–700 K), varied residence depths  
325 (from metal cooling rates), and low Ir concentrations implying differentiation of the injected molten metal.  
326 Their qualitative model of a non-destructive two-body collision agrees with all the available constraints;  
327 however, it requires impact rebound or a similar effect to produce rapid cooling after impact and development  
328 of a megaregolith layer to support later slow cooling (Walte et al., 2020). We show quantitatively that an  
329 intrusion of molten metal into a planetesimal mantle can meet the above constraints without the need for an  
330 impact rebound or development of a late thick megaregolith layer to slow cooling. While our results do not  
331 preclude large-scale changes to the parent body, it removes the need for them; this means that future work  
332 can seek lines of evidence for these planetary-scale processes instead of them being assumed a requirement  
333 for pallasite formation.

334 We show that the required criteria for pallasite formation can be met for a wide range of intrusion  
335 morphologies (Figure 6d), at a wide range of mantle temperatures (as a proxy for both timing of intrusion  
336 and residence depth). For models using planetesimal mantle temperature as initial conditions, criteria were  
337 met more often later in the planetesimal’s history (shortly before the slow metal cooling rates were recorded),  
338 when the mantle was cooler and faster intrusion cooling rates could be achieved (Figure 6a, b); the zoning  
339 preservation requirements cannot be met unless the temperature of the mantle is below 1373 K, as the  
340 intrusion needs to cool below this temperature within 8 years. Small intrusion regions with mean radii  
341 between 20 and 140 m produce the rapid cooling required to preserve olivine chemical heterogeneity (Figure  
342 6c). Similarly, high aspect ratio morphologies (more pipe- or sheet-like) with a minimum radius  $< 50$  m more

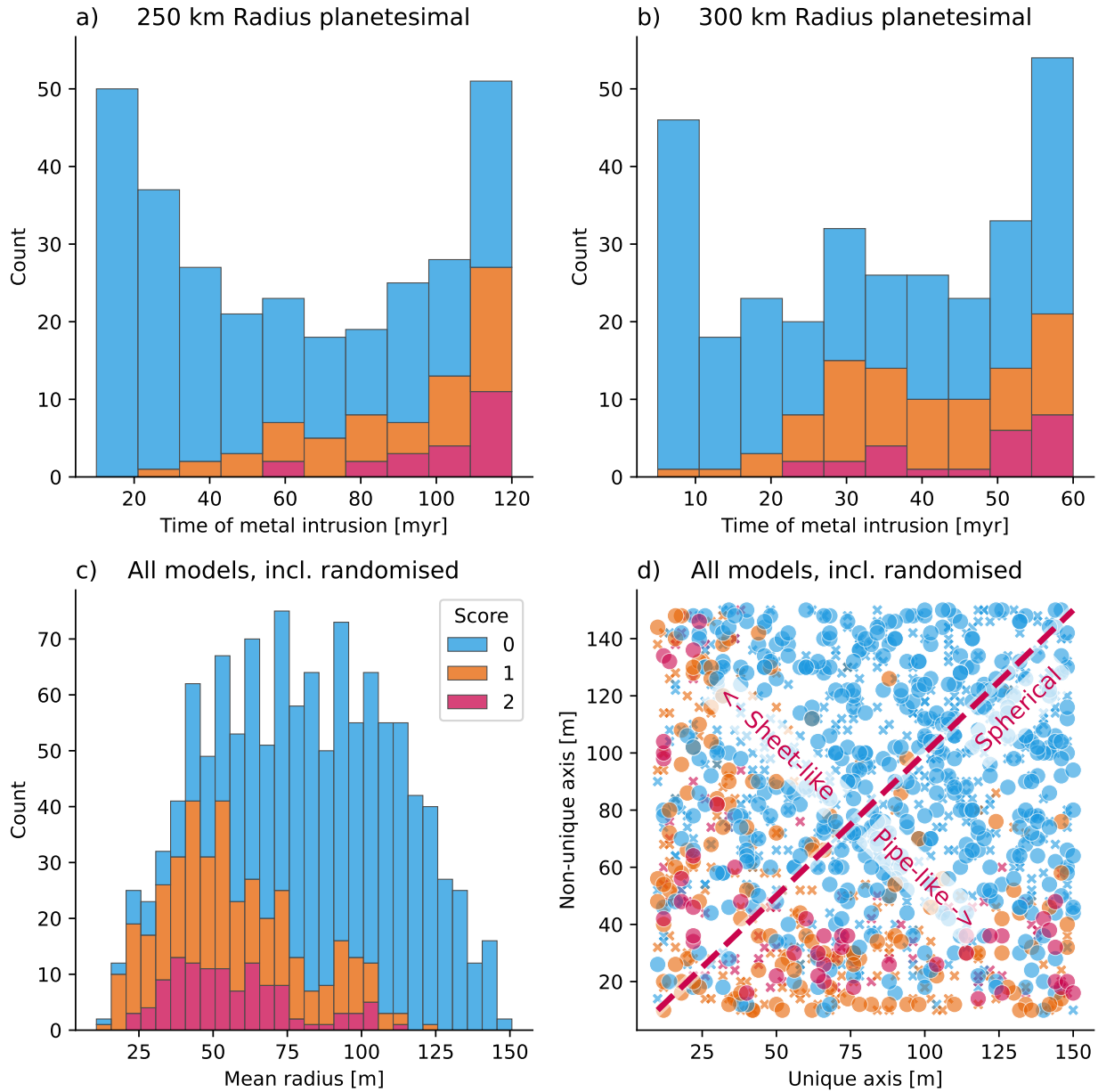


Figure 6: Dependence of score on timing of intrusion, volume of intrusion region, and geometry of intrusion region. a & b) Histograms of score for timing of metal intrusion (in millions of years after initiation of model/crystallisation of magma ocean) for both planetesimal models. Maximum time on both histograms is the time the metal cooling rate was recorded. c) Histograms of score for mean radius of intrusion region for all models with constant material properties (1200 model runs). d) Dependence of score on intrusion region volume and aspect ratio for all models with constant material properties (1200 model runs).

343 frequently meet the constraints as opposed to intrusion segments that are more spherical in shape with both  
344 maximum and minimum radii above  $\sim 50$  m. (Figure 6d), with a weak non-monotonic correlation measured  
345 (Figure S6). This suggests that pallasite-material formation is constrained to intrusions with a sufficiently  
346 small minor axis (of  $\sim 50$  m).

347 In our implementation, the volume of the intrusion region required to satisfy the rounding criteria is  
348 set by the volume (sample mass/average pallasite density) proportion of the meteorite record described as  
349 having angular, rounded, fragmental or mixed textures as the dominant sample texture (Figure S4). This  
350 neglects the variation in density and metal/olivine proportion in samples, varying sulfur content of metal  
351 pockets, and suffers from bias due to a number of outlying massive samples in the record. We bootstrapped  
352 (with replacement) the Meteoritical Bulletin Database (Grossman and Nomenclature Committee of the  
353 Meteoritical Society, 2022) and found the sample size too small to assign robust statistics. We also recognise  
354 that the pallasite meteorite record may not proportionally sample the formation region. However, we apply  
355 the available constraints to our model to show that we can match the meteorite samples available. Despite  
356 these limitations, our model shows that parameters such as the metal fraction of the pallasite region and the  
357 proportion of metal trapped in the planetesimal mantle do not systematically change whether pallasite-like  
358 material can be produced. Our results also highlight the importance of the timing of metal intrusion into the  
359 parent body mantle, and the temperature at which the intruded mantle is residing. Changing the proportion  
360 or volume percentage of rounding required by a small percentage does not change the conclusions of our  
361 study within the parameter range explored: that rounded olivine and preserved chemical zoning can be  
362 recovered from the same pallasite intrusion volume.

363 Hsu (2003) describes calcium zoning in pallasite olivine as ubiquitous, which in combination with detailed  
364 diffusion of Ca in olivine studies, makes it a sensible choice for first steps in calculating erasure or preservation  
365 potential in a metallic intrusion. We set the zoning preservation requirement to  $> 95\%$ , implying that  
366 essentially all pallasites must preserve some degree of Ca heterogeneity. However, we also considered a lower  
367 requirement of  $> 50\%$  to also allow regions of erasure and more intensive diffusional modification (see Figure  
368 S15). Across all model runs, this lower zoning requirement increased the number of model runs that meet  
369 both constraints from 263 (12.0 % of 2200 model runs) to 343 (15.6 % of 2200; see table S2). The same  
370 dependence on mantle temperature and intrusion volume is seen and rapid olivine cooling rates are still met  
371 between four and eight years after intrusion (Figure S9).

372 As mentioned previously, the time and temperature pairings used to estimate grain rounding and zoning  
373 preservation are associated with unquantifiable errors. In order to assess the sensitivity of the model to the  
374 temperature requirements, we varied the temperature of each filter by  $\pm 10\%$  of the original temperature  
375 (Table S2, Figures S12, S13). While the absolute number of successful models changed, the overall relationship

376 between model score and parameters such as initial temperature, background mantle temperature or intrusion  
377 volume remained essentially the same (Figure S14). We also assessed the change through time in intrusion  
378 volume that satisfies each temperature requirement, for the example model run illustrated in Figure 3.  
379 We found that the rounding requirement of  $T_{3\text{mnths}} \geq 1623\text{ K}$  was most strongly dependent on timing of  
380 the measurement, as the intrusion is still rapidly cooling at this time. The intrusion region satisfying this  
381 requirement will change by approximately  $\pm 10$  vol. % per month at this stage in the intrusion process (Figure  
382 S5), whereas by four, eight and ten years when the other temperature requirements must be matched, the  
383 change in the intrusion region that matches each constraint is  $\sim 1$  vol. % or less per month. At three  
384 months, changing the temperature requirement by  $\pm 10$  % may result in a model no longer passing the  
385 rounding criterion (Figure S5); however, this does not change the overall relationship between the input  
386 parameters and the results (Figure S14).

387 The inclusion of a small fraction of metal within the planetesimal mantle may explain the presence of  
388 large (radius  $\sim 5$  mm), well rounded olivine crystals: Saiki et al. (2003) estimated that olivine grains with a  
389 radius of 5 mm would be fully rounded in the presence of FeNi after 7 Myr at or above 1673 K, 29 Myr at or  
390 above 1573 K, or 241 Myr at or above 1473 K. While we primarily focus on models of the pallasite parent  
391 body with a purely olivine mantle, we also modelled a parent body with 15 vol. % metal trapped in the  
392 mantle as in Walte et al. (2020). We assumed that the sole effect of adding this small fraction of metal is to  
393 increase the mantle diffusivity, which in turn accelerates planetary-scale cooling by a small degree (Figure  
394 7). We find that hotter mantles (post magma ocean solidification, with higher olivine solidus temperatures)  
395 better facilitate this large-scale, long term rounding of olivine grains (Figure 7). We also varied the metal  
396 content in the mantle region surrounding the intrusion in our intrusion-scale model between 0–20 vol %, but  
397 found no systematic effect on the score of models (Figure S10).

398 While hotter initial mantle temperatures are required for this earlier period of olivine rounding, the final  
399 stage of metal intrusion that is recorded in pallasites was most likely injected into a cooler mantle that was  
400 approaching  $\sim 800$  K (Figure 6 a, b, Figure 7). We find that intrusions of all sizes into mantles of  $\sim 1200$   
401 K and hotter cannot cool below 1373 K quickly enough to preserve Ca zoning (Figures 4, 7). In order to  
402 reproduce the cooling rates through 873 K suggested by Miyamoto (1997), the background mantle must  
403 be below this temperature at the time of intrusion (Figure 7). This restricts the timing of the pallasite-  
404 forming metal intrusion to between  $\sim 10$ –30 Myr before cooling through the metallographic cooling rates at  
405 approximately 800 K.

406 Our simple model could also be developed by incorporating more complex grain-growth and rounding  
407 mechanisms, such as that of Solferino and Golabek (2018), which focuses on olivine grain growth in contact  
408 with solid Fe-Ni-S at different depths within a planetesimal mantle. While we take a macroscopic approach

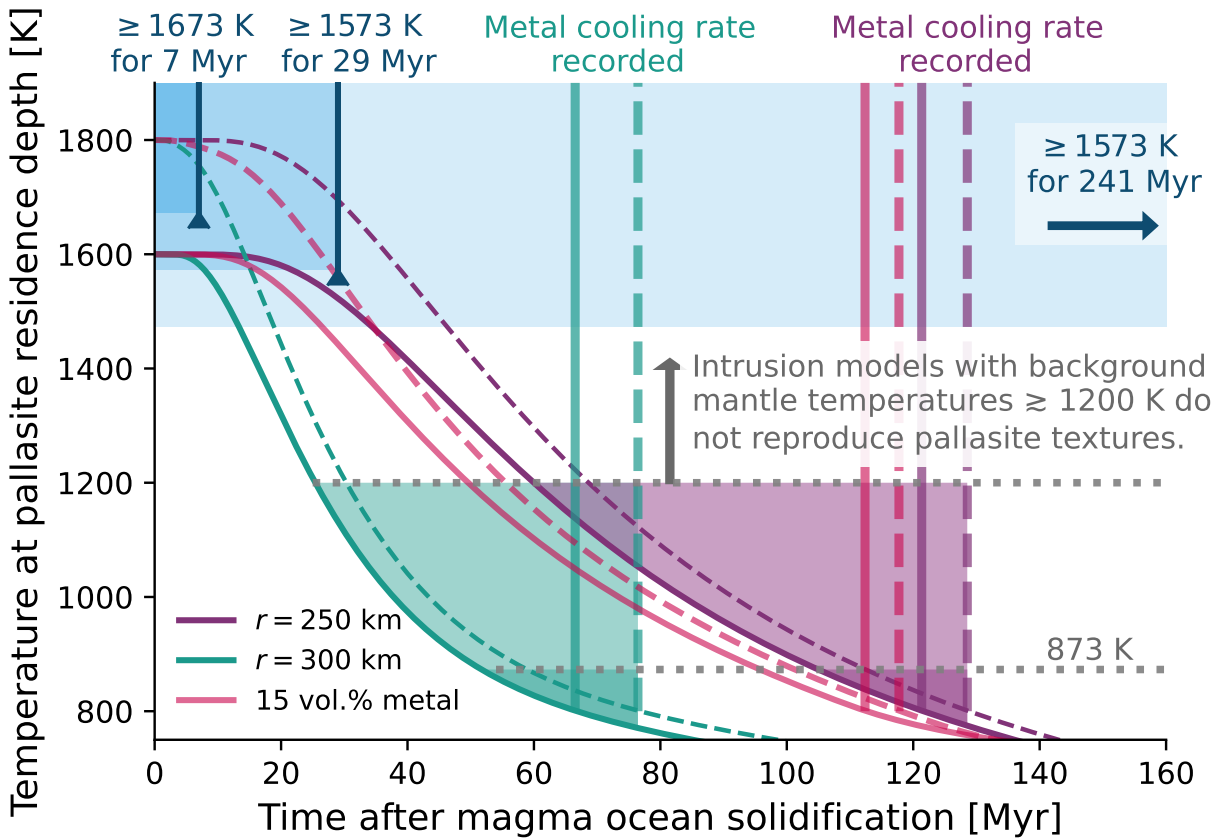


Figure 7: Temperature time series at depth of Imilac pallasite residence, based on FeNi cooling rates (Yang et al., 2010), for a 250 km radius planetesimal with a 125 km radius core (Murphy Quinlan et al., 2021a), a 300 km radius planetesimal with a 200 km radius core (Nichols et al., 2021), and a 250 km radius planetesimal with a 125 km radius core, and 15 % by volume metal trapped in the mantle. Blue boxes represent temperature criteria suggested by Saiki et al. (2003) to explain rounding of large (5 mm radius) olivine crystals; the model cooling time series must pass through one of the blue lines. The two horizontal grey dashed lines indicate maximum background mantle temperature at time of final metal intrusion to meet different criteria: in order to preserve Ca zoning, background mantle temperature must be below 1200 K, which in order to cool through temperature window at the cooling rates suggested by Miyamoto (1997), the background mantle temperature must be below 873 K.

409 to modelling the olivine-metal mixing region, a micro-scale investigation of the crystallisation of metal in  
410 contact with olivine and the potential volume change, localised reactions textures and microstructures would  
411 provide further constraints on the pressure, temperature and time of mixing between these phases.

412 An interesting area of research outside the scope of the current study is the details of metal intrusion  
413 into the parent body mantle and the dominant mode of transport of the metal through the mantle. While  
414 previous models have suggested that the metal may have an internal source (eg., the molten core of the  
415 planetesimal, suggested by a ferrovolcanism origin; Johnson et al., 2020), recent isotopic studies show a  
416 statistically significant disequilibrium between the metal and silicate phases in pallasites, strengthening the  
417 argument for an external source delivered via impact (Windmill et al., 2022). Studies of core formation  
418 via percolative flow (Solferino et al., 2020; Berg et al., 2018) and intrusion propagation and emplacement  
419 (Walker et al., 2021; Stephens et al., 2021) alongside microstructural evidence from pallasite samples can  
420 be utilised to better understand this. Our model can aid in this research, as it provides a range of mantle  
421 temperatures over which pallasite-like textures can be produced.

422 Instead of attempting to recover specific details of the pallasite parent body, we have taken a statistical  
423 approach and instead look at the range of parameters over which pallasite formation is possible. Our results  
424 show that the development of conditions favourable to pallasite formation are common across the parameters  
425 we tested, but are constrained by the mantle temperature, which can be considered a proxy for the timing of  
426 metal intrusion. The two-stage formation hypothesis of Walte and Golabek (2022) suggests that an earlier  
427 impact injected metal into the pallasite parent body mantle, but did not produce “pallasite-like textures” as  
428 observed in meteorite samples, because the mantle was too hot at the time. Instead, the region of intrusion  
429 achieved textural equilibrium, only retaining a small fraction of metal which aided olivine grain growth and  
430 rounding. A later impact is proposed to then deliver more molten metal into the cooler mantle, producing  
431 the textures observed in samples. Our model reproduces the timescales suggested by both these different  
432 stages of formation. These metal-injection events may be a recurrent stage in planetesimal development,  
433 representing a halted core-growth event where cooler mantle temperatures do not facilitate migration of  
434 metal all the way to the centre of the planetesimal before solidification.

435 Framed in this way, perhaps the unusual feature of pallasite meteorites is that they were excavated in  
436 such a way that preserved them and allowed them to be delivered to Earth, as opposed to their formation  
437 being a unique event. This is supported by the evidence for planetesimal growth in two distinct reservoirs  
438 in our Solar System (Morbidelli et al., 2022), both of which are sampled by pallasitic material: while we  
439 specifically discuss and model the parent body of the Main Group Pallasite meteorites, the umbrella group of  
440 pallasites including the Eagle Station Pallasites, the Pyroxene Pallasites, and anomalous ungrouped samples,  
441 must sample multiple parent bodies sourced from both the carbonaceous and non-carbonaceous reservoirs



442 (Jacquet, 2022). These similar lithologies, samples from different regions of the early Solar System, from  
443 isolated planetesimals, suggests that this process was repeated on multiple bodies. Jacquet (2022) suggests  
444 a renaming of the pallasite class to “dunite-iron” meteorites to highlight the textural similarities instead of  
445 inferring a genetic link.

446 It is possible that multiple metal impacts delivered metal to the mantle of the pallasite parent body over  
447 the course of its life span: some of which may have supported core growth during the magma ocean stage  
448 of differentiation; others which stalled in the hot, newly-solidified mantle and eventually reached textural  
449 equilibrium, producing regions of well-rounded, large olivine grains; and later still an intrusion into a cooler  
450 mantle that facilitated rounding of some smaller olivine grains fractured during intrusion, preservation of  
451 chemical heterogeneity in areas previously untouched by prior intrusions, and rapid heating, cooling, and  
452 subsequent diffusional modification of olivine rim compositions. Following this intrusion, the body continued  
453 to cool, the core crystallised and paleomagnetism was recorded in some samples (Bryson et al., 2015; Nichols  
454 et al., 2021; Murphy Quinlan et al., 2021a), and the body became geologically frozen in place until its  
455 destruction  $\sim 100$  Myr ago (Herzog et al., 2015).

## 456 7 Conclusions

457 Different formation environments are not required to explain varied levels of rounding of olivine grains in  
458 pallasite meteorites: large, well-rounded grains may predate metal intrusion and be linked to contact with  
459 primordial metal pockets (Walte et al., 2020) or an earlier injection of metal into a hotter planetesimal  
460 mantle (Walte and Golabek, 2022), while angular grains existed within dunite aggregates away from these  
461 melt pockets before metal intrusion. Fragmental grains may have been fractured during metal intrusion. All  
462 grains in the intrusion region then were rounded according to their location in the intrusion - grains near  
463 the periphery would have cooled rapidly and preserve their initial state (whether well-rounded, fragmental,  
464 or angular), while olivine grains nearer the centre of the intrusion region would cool more slowly, allowing a  
465 greater degree of rounding that would be size-dependent on a macro-scale.

466 Large-scale disruption of, or accretion to, the pallasite parent body are not required to reproduce the  
467 contrasting cooling timescales suggested by olivine and metal diffusion. Instead, the rapid injection of hot  
468 metal into a slowly cooling, warm planetesimal mantle creates a temperature perturbation leading to rapid  
469 initial cooling in the local area, matching that required to preserve olivine compositional heterogeneity,  
470 followed by equilibration with the mantle and a return to the slow planetesimal-scale cooling rates recorded  
471 in the Ni diffusion profiles in the Widmanstätten texture. While Walte and Golabek (2022) suggest that  
472 the pallasite-forming metal intrusion event was aided by still-molten trapped metal pockets, residing in a

473 parent-body mantle above the metal solidus, the later impact and large scale injection of metal could have  
474 re-melted these preexisting FeNi pockets locally, enabling impact into a marginally cooler mantle.

475 Within one small ellipsoidal segment of intrusion, a diversity of textural and diffusive modification of  
476 olivine can be achieved. This does not preclude different formation environments for pallasite meteorites  
477 with differing olivine textures or diffusion profiles, rather it removes this as a requirement. Our simple model  
478 shows that further understanding of the small-scale processes related to the mixing of olivine and metal in  
479 the pallasite region is required to understand the planetesimal-scale processes. The model also highlights the  
480 importance of the temperature of the mantle on the evolution of the pallasite region, and how this is linked  
481 to relative timing of the injection of metal following the crystallisation of the magma ocean, and shows how  
482 different regions of one small intrusion can experience very different temperature-time paths.

483 We produced a simple, first-step model to address the contrasting timescales preserved in pallasite  
484 meteorites and suggest that the simplest explanation (injection of metal into the mantle of a planetesimal)  
485 without ad hoc changes to the parent body, can explain the heterogeneity seen across pallasite meteorites.  
486 We suggest that pallasite meteorites represent a late, preserved metallic intrusion into a planetesimal mantle  
487 and speculate that this parent body potentially experienced earlier metal-injections: previous intrusions  
488 would have delivered material to the core, leaving a small fraction trapped within the mantle.

## 489 Acknowledgements

490 M. Murphy Quinlan was supported by the Leeds-York Natural Environment Research Council Doctoral  
491 Training Partnership (NE/L002574/1). C. J. Davies was supported by Natural Environment Research  
492 Council Grant (NE/V010867/1).

## 493 References

- 494 M. T. L. Berg, G. D. Bromiley, Y. Le Godec, J. Philippe, M. Mezouar, J.-P. Perrillat,  
495 and N. J. Potts. Rapid core formation in terrestrial planets by percolative flow: In-  
496 situ imaging of metallic melt migration under high pressure/temperature conditions.  
497 *Frontiers in Earth Science*, 6:77, Jun 2018. doi: 10.3389/feart.2018.00077. URL  
498 <https://www.frontiersin.org/article/10.3389/feart.2018.00077/full>.
- 499 J. S. Boesenberg, J. S. Delaney, and R. H. Hewins. A petrological and chemical reexamination of  
500 main group pallasite formation. *Geochimica et Cosmochimica Acta*, 89:134–158, July 2012. doi:  
501 10.1016/j.gca.2012.04.037. URL <https://doi.org/10.1016/j.gca.2012.04.037>.

502 D. T. Britt and G. J. S. J. Consolmagno. Stony meteorite porosities and densities: A review  
503 of the data through 2001. *Meteoritics & Planetary Science*, 38(8):1161–1180, 2003. doi:  
504 <https://doi.org/10.1111/j.1945-5100.2003.tb00305.x>.

505 J. F. J. Bryson, C. I. O. Nichols, J. Herrero-Albillos, F. Kronast, T. Kasama, H. Alimadadi, G. van der  
506 Laan, F. Nimmo, and R. J. Harrison. Long-lived magnetism from solidification-driven convection on the  
507 pallasite parent body. *Nature*, 517(7535):472–475, 2015. doi: 10.1038/nature14114.

508 H. S. Carslaw and J. C. Jaeger. *Conduction of heat in solids*. Clarendon Press ; Oxford University Press,  
509 Oxford : New York, 2nd edition, 1959.

510 W. Cen, R. Hoppe, and N. Gu. Fast and accurate determination of 3D temperature distribution using  
511 fraction-step semi-implicit method. *AIP Advances*, 6(9):095305, 2016. doi: 10.1063/1.4962665.

512 S. M. Chernozhkin, S. J. McKibbin, S. Goderis, S. J. M. Van Malderen, P. Claeys, and F. Vanhaecke.  
513 New constraints on the formation of main group pallasites derived from in situ trace element  
514 analysis and 2D mapping of olivine and phosphate. *Chemical Geology*, 562:119996, 2021. doi:  
515 10.1016/j.chemgeo.2020.119996.

516 J. Crank and P. Nicolson. A practical method for numerical evaluation of solutions of partial differential  
517 equations of the heat-conduction type. *Mathematical Proceedings of the Cambridge Philosophical Society*,  
518 43(1):50–67, 1947. doi: 10.1017/s0305004100023197.

519 E. G. Ehlers. *The Interpretation of Geological Phase Diagrams*. W. H. Freeman and Co., Ltd., 1972.

520 J. I. Goldstein, J. Yang, and E. R. Scott. Determining cooling rates of iron and  
521 stony-iron meteorites from measurements of Ni and Co at kamacite–taenite interfaces.  
522 *Geochimica et Cosmochimica Acta*, 140:297–320, 2014. doi: 10.1016/j.gca.2014.05.025. URL  
523 <https://linkinghub.elsevier.com/retrieve/pii/S0016703714003548>.

524 J. Grossman and Nomenclature Committee of the Meteoritical Society. Meteoritical Bulletin Database.  
525 <https://www.lpi.usra.edu/meteor/>, 2022. Accessed: 2022-02-26.

526 G. F. Herzog, D. L. Cook, M. Cosarinsky, L. Huber, I. Leya, and J. Park. Cosmic-ray exposure ages  
527 of pallasites. *Meteoritics & Planetary Science*, 50(1):86–111, 2015. doi: 10.1111/maps.12404. URL  
528 <https://onlinelibrary.wiley.com/doi/abs/10.1111/maps.12404>.

529 W. Hsu. Minor element zoning and trace element geochemistry of pallasites. *Meteoritics & Planetary Science*,  
530 38(8):1217–1241, 2003. ISSN 10869379, 19455100. doi: 10.1111/j.1945-5100.2003.tb00309.x.

- 531 E. Jacquet. Meteorite petrology versus genetics: Toward a unified binominal classification. *Meteoritics &*  
532 *Planetary Science*, 57(9):1774–1794, 2022. doi: <https://doi.org/10.1111/maps.13896>.
- 533 B. C. Johnson, M. M. Sori, and A. J. Evans. Ferrovulcanism on metal worlds and the origin  
534 of pallasites. *Nature Astronomy*, 4(1):41–44, 2020. doi: 10.1038/s41550-019-0885-x. URL  
535 <http://www.nature.com/articles/s41550-019-0885-x>.
- 536 A. J. G. Jurewicz and E. B. Watson. Cations in olivine, Part 2: Diffusion in olivine xenocrysts, with  
537 applications to petrology and mineral physics. *Contributions to Mineralogy and Petrology*, 99(2):186–201,  
538 1988. doi: 10.1007/BF00371460.
- 539 H. P. Langtangen and S. Linge. *Finite Difference Computing with PDEs*. Springer International Publishing,  
540 2017. doi: 10.1007/978-3-319-55456-3. URL <https://doi.org/10.1007/978-3-319-55456-3>.
- 541 S. J. McKibbin, L. Pittarello, C. Makarona, C. Hamann, L. Hecht, S. M. Chernozhkin, S. Goderis,  
542 and P. Claeys. Petrogenesis of main group pallasite meteorites based on relationships among texture,  
543 mineralogy, and geochemistry. *Meteoritics & Planetary Science*, 54(11):2814–2844, 2019. doi:  
544 10.1111/maps.13392. URL <https://onlinelibrary.wiley.com/doi/abs/10.1111/maps.13392>.
- 545 M. Miyamoto. Chemical zoning of olivine in several pallasites. *Journal of Geophysical Research: Planets*,  
546 102(E9):21613–21618, 1997. doi: 10.1029/97JE01852.
- 547 A. Morbidelli, K. Baillié, K. Batygin, S. Charnoz, T. Guillot, D. C. Rubie, and T. Kleine. Contemporary  
548 formation of early solar system planetesimals at two distinct radial locations. *Nature Astronomy*, 6(1):  
549 72–79, 2022. doi: 10.1038/s41550-021-01517-7.
- 550 D. Mottaghy and V. Rath. Latent heat effects in subsurface heat transport modelling and their impact  
551 on palaeotemperature reconstructions. *Geophysical Journal International*, 164(1):236–245, 2006. doi:  
552 10.1111/j.1365-246x.2005.02843.x.
- 553 M. Murphy Quinlan, A. M. Walker, C. J. Davies, J. E. Mound, T. Müller, and J. Harvey. The Conductive  
554 Cooling of Planetesimals With Temperature-Dependent Properties. *Journal of Geophysical Research:*  
555 *Planets*, 126(4), 2021a. doi: 10.1029/2020JE006726.
- 556 M. Murphy Quinlan, A. M. Walker, P. Selves, and L. S. E. Teggin. Pytesimal software package: v2.0.0,  
557 2021b.
- 558 C. I. O. Nichols, J. F. J. Bryson, R. D. Cottrell, R. R. Fu, R. J. Harrison, J. Herrero-Albillos, F. Kronast,  
559 J. A. Tarduno, and B. P. Weiss. A Time-Resolved Paleomagnetic Record of Main Group Pallasites:

560 Evidence for a Large-Cored, Thin-Mantled Parent Body. *Journal of Geophysical Research: Planets*, 126  
561 (7):e2021JE006900, 2021. doi: <https://doi.org/10.1029/2021JE006900>.

562 M. Özisik. *Heat conduction*. Wiley, New York, 1993.

563 K. Saiki, D. Laporte, D. Vielzeuf, S. Nakashima, and P. Boivin. Morphological analysis of olivine grains  
564 annealed in an iron-nickel matrix: Experimental constraints on the origin of pallasites and on the thermal  
565 history of their parent bodies. *Meteoritics & Planetary Science*, 38(3):427–444, 2003.

566 G. F. Solferino and G. J. Golabek. Olivine grain growth in partially molten fe–ni–s: A proxy for the genesis  
567 of pallasite meteorites. *Earth and Planetary Science Letters*, 504:38–52, 2018. Publisher: Elsevier.

568 G. F. D. Solferino, P.-R. Thomson, and S. Hier-Majumder. Pore network modeling of core forming melts  
569 in planetesimals. *Frontiers in Earth Science*, 8:339, Aug 2020. doi: 10.3389/feart.2020.00339. URL  
570 <https://www.frontiersin.org/article/10.3389/feart.2020.00339/full>.

571 T. Stephens, R. Walker, D. Healy, and A. Bubeck. Segment tip geometry of sheet  
572 intrusions, ii: Field observations of tip geometries and a model for evolving emplacement  
573 mechanisms. *Volcanica*, 4(2):203–225, Oct 2021. doi: 10.30909/vol.04.02.203225. URL  
574 <https://www.jvolcanica.org/ojs/index.php/volcanica/article/view/109>.

575 J. A. Tarduno, R. D. Cottrell, F. Nimmo, J. Hopkins, J. Voronov, A. Erickson, E. Blackman,  
576 E. R. Scott, and R. McKinley. Evidence for a dynamo in the main group pallasite  
577 parent body. *Science*, 338(6109):939–942, 2012. doi: 10.1126/science.1223932. URL  
578 <https://www.science.org/doi/abs/10.1126/science.1223932>.

579 T. Tomiyama and G. R. Huss. Minor and trace element zoning in pallasite olivine: modeling pallasite  
580 thermal history. *Lunar Planet.Sci.*, 37:2132, 2006. URL [www.scopus.com](http://www.scopus.com). Cited By :3.

581 R. Walker, T. Stephens, C. Greenfield, S. Gill, D. Healy, and S. Poppe. Segment tip geometry  
582 of sheet intrusions, i: Theory and numerical models for the role of tip shape in controlling  
583 propagation pathways. *Volcanica*, 4(2):189–201, Oct 2021. doi: 10.30909/vol.04.02.189201. URL  
584 <https://www.jvolcanica.org/ojs/index.php/volcanica/article/view/114>.

585 N. P. Walte and G. J. Golabek. Olivine aggregates reveal a complex collisional history of the main group  
586 pallasite parent body. *Meteoritics & Planetary Science*, 57(5):1098–1115, 2022. doi: 10.1111/maps.13810.  
587 URL <https://onlinelibrary.wiley.com/doi/abs/10.1111/maps.13810>.

- 588 N. P. Walte, G. F. D. Solferino, G. J. Golabek, D. Silva Souza, and A. Bouvier. Two-stage formation  
589 of pallasites and the evolution of their parent bodies revealed by deformation experiments. *Earth and*  
590 *Planetary Science Letters*, 546:116419, 2020. ISSN 0012-821X. doi: 10.1016/j.epsl.2020.116419.
- 591 R. J. Windmill, I. A. Franchi, J. L. Hellmann, J. M. Schneider, F. Spitzer, T. Kleine, R. C. Greenwood,  
592 and M. Anand. Isotopic evidence for pallasite formation by impact mixing of olivine and metal  
593 during the first 10 million years of the solar system. *PNAS Nexus*, 1(1):pgac015, Mar 2022. doi:  
594 10.1093/pnasnexus/pgac015. URL <https://doi.org/10.1093/pnasnexus/pgac015>.
- 595 N. N. Yanenko. *The Method of Fractional Steps*. Springer Berlin Heidelberg, 1971. doi: 10.1007/978-3-642-  
596 65108-3.
- 597 C. W. Yang, D. B. Williams, and J. I. Goldstein. A new empirical cooling rate indicator for meteorites based  
598 on the size of the cloudy zone of the metallic phases. *Meteoritics & Planetary Science*, 32(3):423–429,  
599 1997.
- 600 J. Yang, J. I. Goldstein, and E. R. Scott. Main-group pallasites: Thermal history, relationship to IIIAB  
601 irons, and origin. *Geochimica et Cosmochimica Acta*, 74(15):4471–4492, 2010. ISSN 0016-7037. doi:  
602 10.1016/j.gca.2010.04.016.
- 603 M. Zeneli, A. Nikolopoulos, S. Karellas, and N. Nikolopoulos. Numerical methods for solid-liquid phase-  
604 change problems. In *Ultra-High Temperature Thermal Energy Storage, Transfer and Conversion*, pages  
605 165–199. Elsevier, 2021. doi: 10.1016/b978-0-12-819955-8.00007-7.

# Supplementary materials for: Reconciling fast and slow cooling during planetary formation as recorded in the main group pallasites

M. Murphy Quinlan\*<sup>1</sup>      A. M. Walker<sup>2</sup>      C. J. Davies<sup>1</sup>

\*Email: eememq@leeds.ac.uk

<sup>1</sup>*School of Earth and Environment, University of Leeds, Leeds, UK*

<sup>2</sup>*Department of Earth Sciences, University of Oxford, Oxford, UK*

March 27, 2023

## 1 Extended methods

Our intrusion model consists of an ellipsoid region of interconnected solid olivine bridgework (Boesenberg et al., 2012), the pore space (created by inter- and intra-granular fractures) of which has been infiltrated and saturated by initially molten metal. This intrusion region is surrounded by a portion of the planetesimal mantle. We assume convection of the metal in this region is inhibited by the low porosity and permeability of the solid olivine bridgework, the rapid crystallisation of the metal, and the low gravitational acceleration.

We consider a cartesian box of mantle material with constant temperature in the horizontal directions  $x$  and  $y$ , and the vertical coordinate  $z$  aligned with the 1D mantle temperature output from the planetesimal model. Assuming a purely conductive system in which convective heat transport and internal heat generation are neglected, the temperature  $T$  (K) in this volume satisfies the three-dimensional heat conduction equation (Carslaw and Jaeger, 1959):

$$\rho c_p \frac{\partial T}{\partial t} = \frac{\partial}{\partial x} \left( k \frac{\partial T}{\partial x} \right) + \frac{\partial}{\partial y} \left( k \frac{\partial T}{\partial y} \right) + \frac{\partial}{\partial z} \left( k \frac{\partial T}{\partial z} \right) \quad (1)$$

where:  $\rho$  is the density of the material ( $\text{kg m}^{-3}$ );  $c_p$  is the specific heat capacity ( $\text{J kg}^{-1} \text{K}^{-1}$ );  $t$  is time (s);  $x$ ,  $y$ , and  $z$  are the spatial coordinates (m); and  $k$  is thermal conductivity ( $\text{W m}^{-1} \text{K}^{-1}$ ). We choose temperature-independent  $k$ , allowing the Crank-Nicolson scheme to be applied to the problem without the complications associated with non-linearity (Carslaw and Jaeger, 1959; Özisik, 1993).

We define a uniaxial ellipsoid centered in the box, of volume  $V = \frac{4}{3}\pi a^2 b$ , where  $a$  and  $b$  are radii, which represents the intrusion region with a pallasitic mix of silicate and metal. The dimensions of the box ( $X = Y = Z$ ) enclosing this ellipsoid is set by the diffusion lengthscale for the mantle material: we wish to

19 run the model for ten years, and do not want the temperature near the model boundaries to change during  
 20 that time. This allows us to apply a zero-flux condition to the boundaries of the problem.

21 Directly modelling the mixed-phase region of olivine crystals and metal melt would be computationally  
 22 expensive and require detailed knowledge of the geometry of the phase mixture. Instead, we take a  
 23 macroscopic approach to track the cooling and crystallisation of the metal in this area, and consider the  
 24 intrusion region as a homogeneous, isotropic material, using volume-averaged effective thermal properties.  
 25 We adopt the method of Mottaghy and Rath (2006) to model permafrost: we assume a simple saturated two  
 26 component system, where olivine forms a solid interconnected bridgework of crystals, with the pore space  
 27 filled with metal.

28 The volume fraction of metal-saturated pore space is denoted by  $\phi_m$ , while the olivine fraction is labelled  
 29  $\phi_{ol}$ , with  $\phi_{ol} + \phi_m = 1$ . We can then replace  $\rho c_p$  in equation 1 with the arithmetic mean of  $\rho c_p$  for metal  
 30 and olivine ( $\rho_m c_m$  and  $\rho_{ol} c_{ol}$ ), and  $k$  with the square-root mean for both phases ( $k_m$  and  $k_{ol}$ ) as this is more  
 31 physically realistic for a randomly distributed mixture (Mottaghy and Rath, 2006; Roy et al., 1981):

$$\rho c_p = \phi_m \rho_m c_m + \phi_{ol} \rho_{ol} c_{ol}, \quad k = \left( \phi_m \sqrt{k_m} + \phi_{ol} \sqrt{k_{ol}} \right)^2. \quad (2)$$

32 The metal-filled porosity can be further divided into the solid ( $\phi_{m(s)}$ ) and liquid ( $\phi_{m(l)}$ ) fractions:

$$\phi_m = \phi_{m(s)} + \phi_{m(l)}. \quad (3)$$

33 The fraction of solid and liquid metal is controlled by a temperature-dependent function which should  
 34 be one when the metal is entirely solid ( $T < T_S$ , the solidus temperature), and zero when the metal is fluid  
 35 ( $T > T_L$ , the liquidus temperature). We use the differentiable equation suggested by Mottaghy and Rath  
 36 (2006):

$$\Theta = \begin{cases} \exp \left[ - \left( \frac{T-T_L}{w} \right)^2 \right] & \text{if } T < T_L, \\ 1 & \text{if } T > T_L, \end{cases} \quad (4)$$

37 where  $w$  is just  $\frac{\Delta T}{2} = \frac{T_L - T_S}{2}$ . This is differentiable:

$$\frac{d\Theta}{dT} = \begin{cases} -\frac{2(T-T_L)}{w^2} \exp \left[ - \left( \frac{T-T_L}{w} \right)^2 \right] & \text{if } T \leq T_L, \\ 0 & \text{if } T > T_L. \end{cases} \quad (5)$$

38 We apply this to the crystallisation of meteoritic Fe-Ni-S metal (Fig. S1), with  $T_L = 1600$  K and



39  $T_S = 1260$  K (Wasson and Choi, 2003, Ehlers, 1972).

40 To account for the latent heat associated with melting or crystallisation, we apply the simple fixed-domain  
 41 apparent heat capacity method which correlates the heat capacity of the phase-changing material with the  
 42 slope of the enthalpy-temperature curve (Zeneli et al., 2021). We add a term to the heat capacity of the  
 43 component that experiences the phase change—in this case, the metal—to define a new apparent volumetric  
 44 heat capacity ( $\rho c_{m,app}$ ; Sarbu and Sebarchievici, 2017):

$$\phi_m \rho c_{m,app} = \phi_{m(l)} \rho_{m(l)} c_{m(l)} + \phi_{m(s)} \rho_{m(s)} c_{m(s)} + \rho_{m(l)} L \frac{\partial \phi_{m(l)}}{\partial T}, \quad (6)$$

45 where  $L$  is the specific latent heat of fusion ( $\text{J kg}^{-1}$ ). This can then be substituted in to equation 2 to  
 46 find the overall apparent heat capacity of the mixed region; similarly, the conductivity can be modified to  
 47 accommodate the solid and liquid metal phase. Diffusivity ( $\kappa$ ,  $\text{m}^2 \text{s}^{-1}$ ) can be defined for all the phases in  
 48 the mixed region, including the phase change effects:

$$\kappa = \frac{k}{\rho c_p} = \frac{(\phi_{m(l)} \sqrt{k_{m(l)}} + \phi_{m(s)} \sqrt{k_{m(s)}} + \phi_{ol} \sqrt{k_{ol}})^2}{\phi_{m(l)} \rho_{m(l)} c_{m(l)} + \phi_{m(s)} \rho_{m(s)} c_{m(s)} + \rho_{m(l)} L \frac{\partial \phi_{m(l)}}{\partial T} + \phi_{ol} \rho_{ol} c_{ol}}. \quad (7)$$

49 While diffusivity inside the ellipsoidal intrusion region is defined by equation 7, the material properties  
 50 outside the intrusion have either constant values that match that of olivine, or use the same equations but  
 51 with a smaller fraction of metal (to approximate metal trapped in the mantle). Sudden jumps and step  
 52 functions in the spatially-varying diffusivity can introduce instabilities especially if these material properties  
 53 boundaries intersect with the model boundary. We ensure this does not happen by centering our intrusion  
 54 ellipsoid within mantle material with spatially-constant material properties, so that the model boundary  
 55 never crosses the mantle-intrusion boundary.

## 56 1.1 Numerical approach

57 To illustrate our approach, we first consider the heat equation in 1D and write it in terms of spatially varying  
 58 diffusivity:

$$\frac{\partial T}{\partial t} = \frac{\partial}{\partial x} \left( \kappa(x) \frac{\partial T}{\partial x} \right) + \text{I.B.C.}, \quad (8)$$

59 where I.B.C. stands for initial and boundary conditions. We apply the semi-implicit Crank-Nicolson scheme  
 60 (Crank and Nicolson, 1947) with zero-flux boundary conditions. Forward difference is used for the time  
 61 derivative of  $T$ , and the spatial derivative is evaluated at the time step  $n + 1/2$  instead of at  $n$ , taking the  
 62 arithmetic mean between the time step  $n$  and  $n + 1$ . We also discretise  $\kappa$  with respect to distance,  $i$ , using

63 finite differences (Langtangen and Linge, 2017).

64 After expansion and simplification, the resulting system of linear equations can be represented in matrix  
65 form:  $A\mathbf{T}^{n+1} + \mathbf{b}^{n+1} = B\mathbf{T}^n + \mathbf{b}^n$ , where  $A$  and  $B$  are  $N \times N$  matrices,  $\mathbf{T}^{n+1}$  and  $\mathbf{T}^n$  are column vectors of  
66 temperature at times  $n + 1$  and  $n$ , and  $\mathbf{b}^n$  and  $\mathbf{b}^{n+1}$  are boundary condition column vectors. For zero-flux  
67 boundary conditions, these column vectors are zero. We define a new parameter in place of the Fourier  
68 number, with variable diffusivity:  $\mathbf{r}_i = \kappa_i \Delta t / \Delta x^2$ , where  $\Delta t$  is the time step and  $\Delta x$  is the spatial step. We  
69 can then define the upper, lower and diagonal coefficients of  $A$  and  $B$ :

$$\begin{aligned} R_i^U &= r_i + r_{i+1}, \\ R_i^L &= r_i + r_{i-1}, \\ R_i^D &= 2r_i + r_{i+1} + r_{i-1}. \end{aligned} \tag{9}$$

70 The matrix equation can then be written:

$$\begin{aligned} & \begin{pmatrix} 4 + R_0^D & -2R_0^U & & & & \\ -R_1^L & 4 + R_1^D & -r_1 & & & \\ & & \ddots & & & \\ & & & 0 & -R_{N-1}^L & 4 + R_{N-1}^D & -R_{N-1}^U \\ & & & & -2R_N^L & 4 + R_N^D & \end{pmatrix} \begin{pmatrix} T_0^{n+1} \\ T_1^{n+1} \\ \vdots \\ T_{N-1}^{n+1} \\ T_N^{n+1} \end{pmatrix} \\ = & \begin{pmatrix} 4 - R_0^D & 2R_0^U & & & & \\ R_1^L & 4 - R_1^D & R_1^U & & & \\ & & \ddots & & & \\ & & & 0 & R_{N-1}^U & 4 - R_{N-1}^D & R_{N-1}^L \\ & & & & 2R_N^L & 4 - R_N^D & \end{pmatrix} \begin{pmatrix} T_0^n \\ T_1^n \\ \vdots \\ T_{N-1}^n \\ T_N^n \end{pmatrix}. \end{aligned} \tag{10}$$

71 This requires that  $\mathbf{r}$  is a column vector with two ghost points at  $r_{-1}$  and  $r_{N+1}$ . In order to find the  
72 temperature distribution at the next time step, we multiply across by the inverse of  $A$ :  $\mathbf{T}_i^{n+1} = (A^{-1}B)\mathbf{T}_i^n$ .  
73 The full derivation of these matrix equations can be found in the supplementary information.

74 In order to extend this scheme to three dimensions, we apply the Fractional Step Method (Cen et al.,  
75 2016; Yanenko, 1971), which evaluates the heat equation in one-third time step increments along each of the  
76 spatial dimensions  $i$ ,  $j$  and  $k$ :

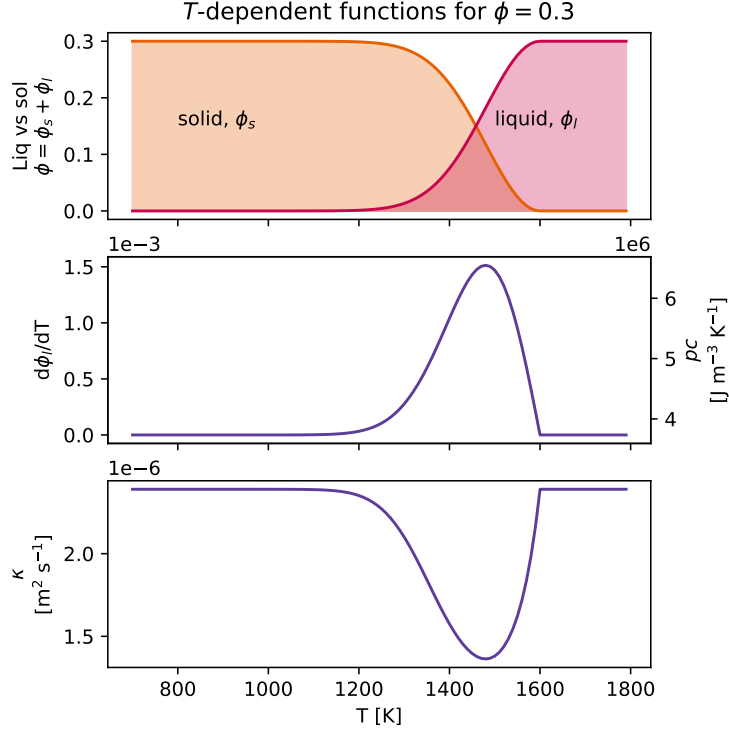


Figure S1: Temperature dependent functions for a mixed region of 30 % phase-change material (PCM - in this case, metal -  $\phi$ ), and 70 % non-PCM, in this case olivine ( $1 - \phi$ ). The functions for  $\kappa$  and  $\rho c$  are for this mixture. To simplify the problem, we have set the material properties for liquid and solid metal as equal; however, the code allows these to be varied independently.

$$\begin{aligned}
 A\mathbf{T}_{j,k}^{n+\frac{1}{3}} &= B\mathbf{T}_{j,k}^n, \\
 A\mathbf{T}_{i,k}^{n+\frac{2}{3}} &= B\mathbf{T}_{i,k}^{n+\frac{1}{3}}, \\
 A\mathbf{T}_{i,j}^{n+1} &= B\mathbf{T}_{i,j}^{n+\frac{2}{3}},
 \end{aligned} \tag{11}$$

77 where the superscript  $(n + \frac{1}{3})$  refers to the fractional time step  $t^{n+\frac{1}{3}} = t^n + \frac{1}{3}\Delta t$  and so on. The temperature  
 78 distribution at the next time step is found by evaluating these three one-dimensional equations in turn instead  
 79 of one three-dimensional equation (Sahijpal, 2021).

80 We bench-marked our numerical model against an analytical solution from Carslaw and Jaeger (1959),  
 81 and found that the maximum relative defect between the numerical and analytical models dropped to below  
 82 1 % within 150 seconds (Figure S2).

## 83 2 Additional figures relating to benchmarking and sensitivity analyses

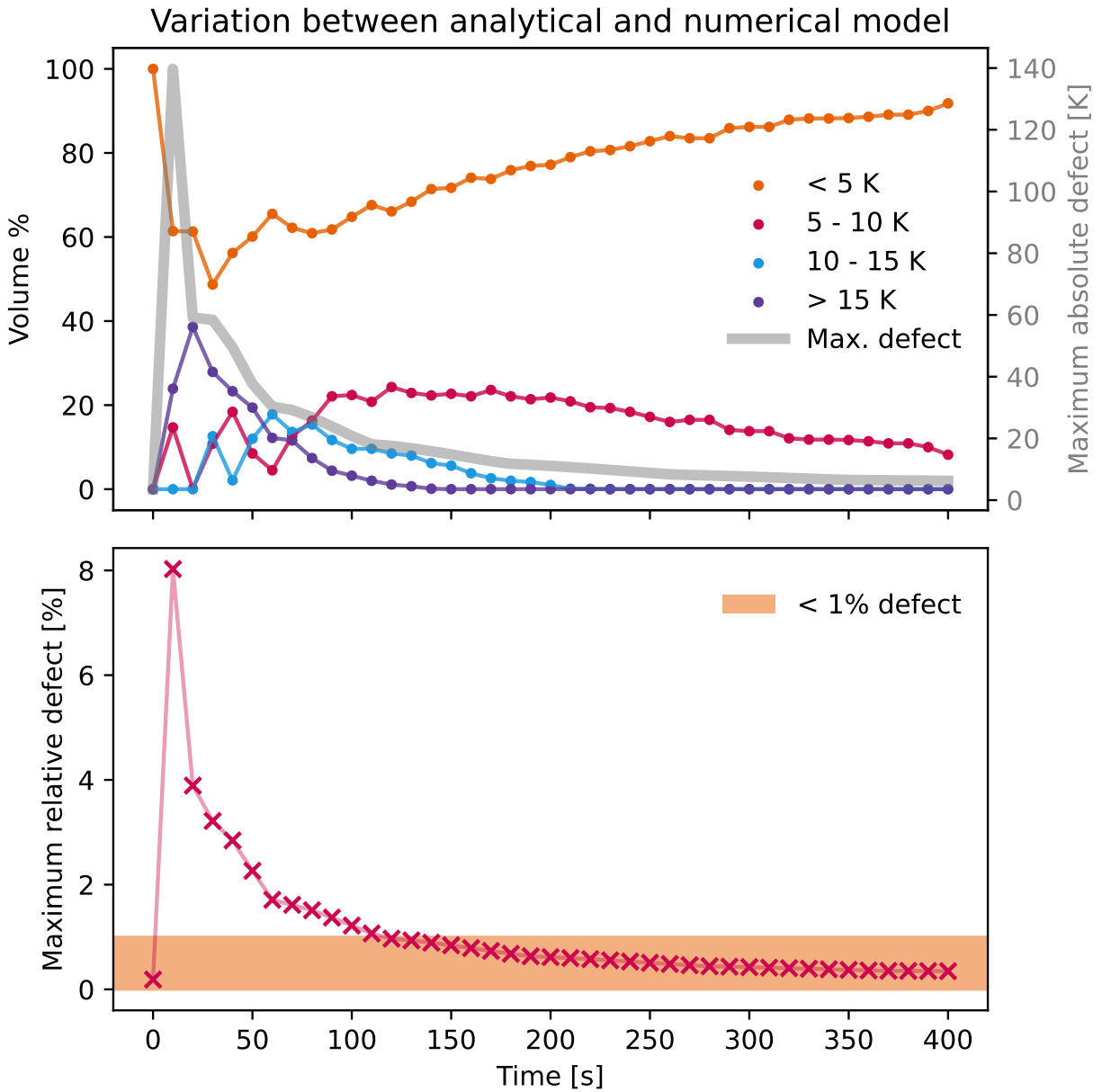


Figure S2: The numerical model was set up to closely approximate a cube with fixed-temperature boundary conditions and spatially constant diffusivity, and the results were compared to the output of an analytical solution for the same geometry (Carslaw and Jaeger, 1959). Within 150 seconds, the maximum relative defect drops below 1 %, with the majority of the numerically modelled region within 5 K of the analytical solution (comparing pixel to equivalent pixel).

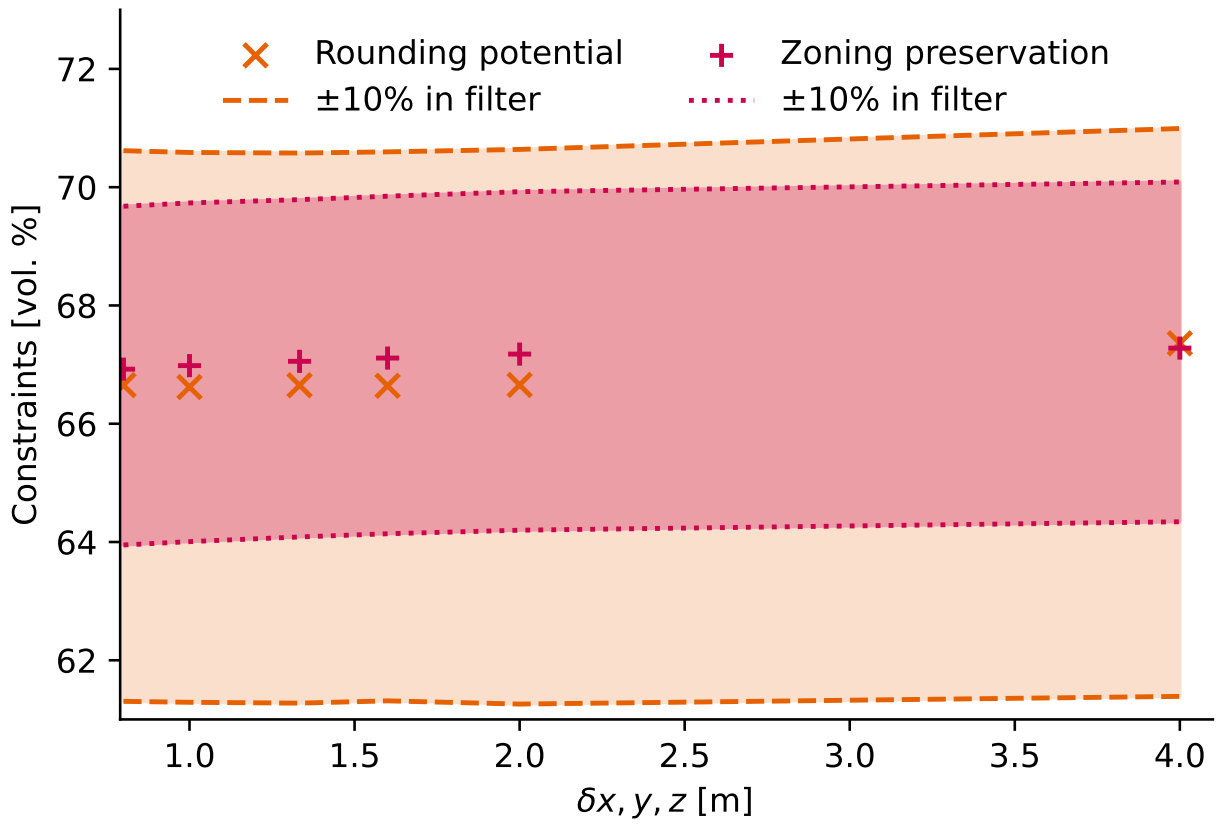


Figure S3: Exploration of effect of model resolution and rounding potential/zoning preservation. Spatial step size of  $< 4$  m results in a change in either result by  $< 1\%$ . These are compared to the effect of increasing or decreasing the temperature cutoffs for the rounding and zoning criteria.

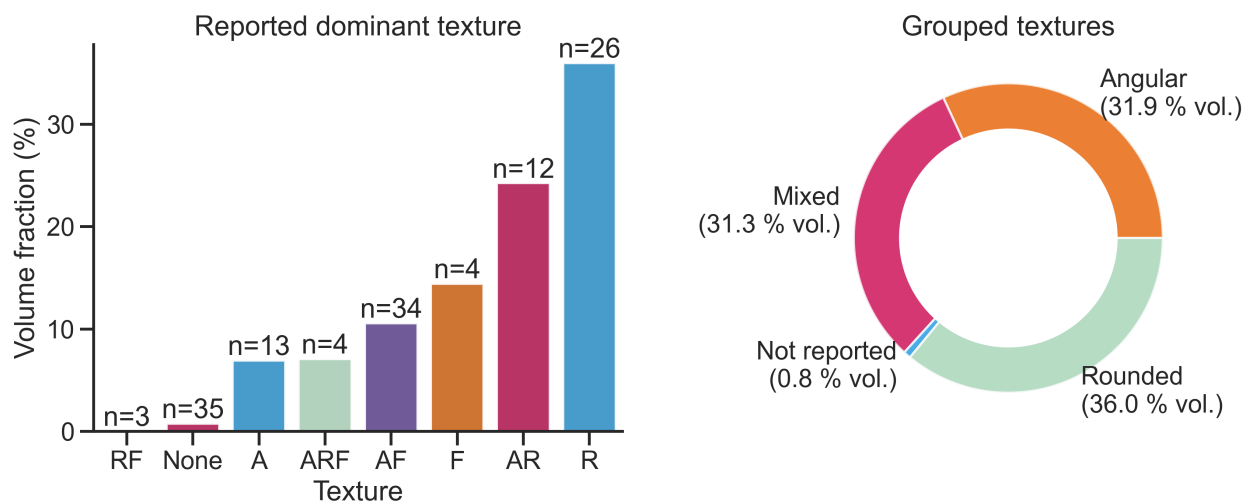


Figure S4: Pallasite olivine macro-textures based on qualitative descriptions from the Meteoritical Bulletin and collated results from McKibbin et al. (2019), shown as volume fraction of the total pallasite record. RF: rounded fragmented; None: no texture mentioned in description; A: angular; ARF: mixed texture; AF: angular fragmental; F: fragmental; AR: mixed texture; R: rounded. The pie chart shows these grouped as used in the model constraints, with groups A and AF combined into “Angular”, and groups RF, ARF and AR combined into “Mixed”. “Rounded” contains only the group R. For the model to “pass” the rounding constraint, the volume that can potentially support rounding needs to fall between “Rounded” (36 vol. %) and “Rounded” + “Mixed” (67 vol. %).

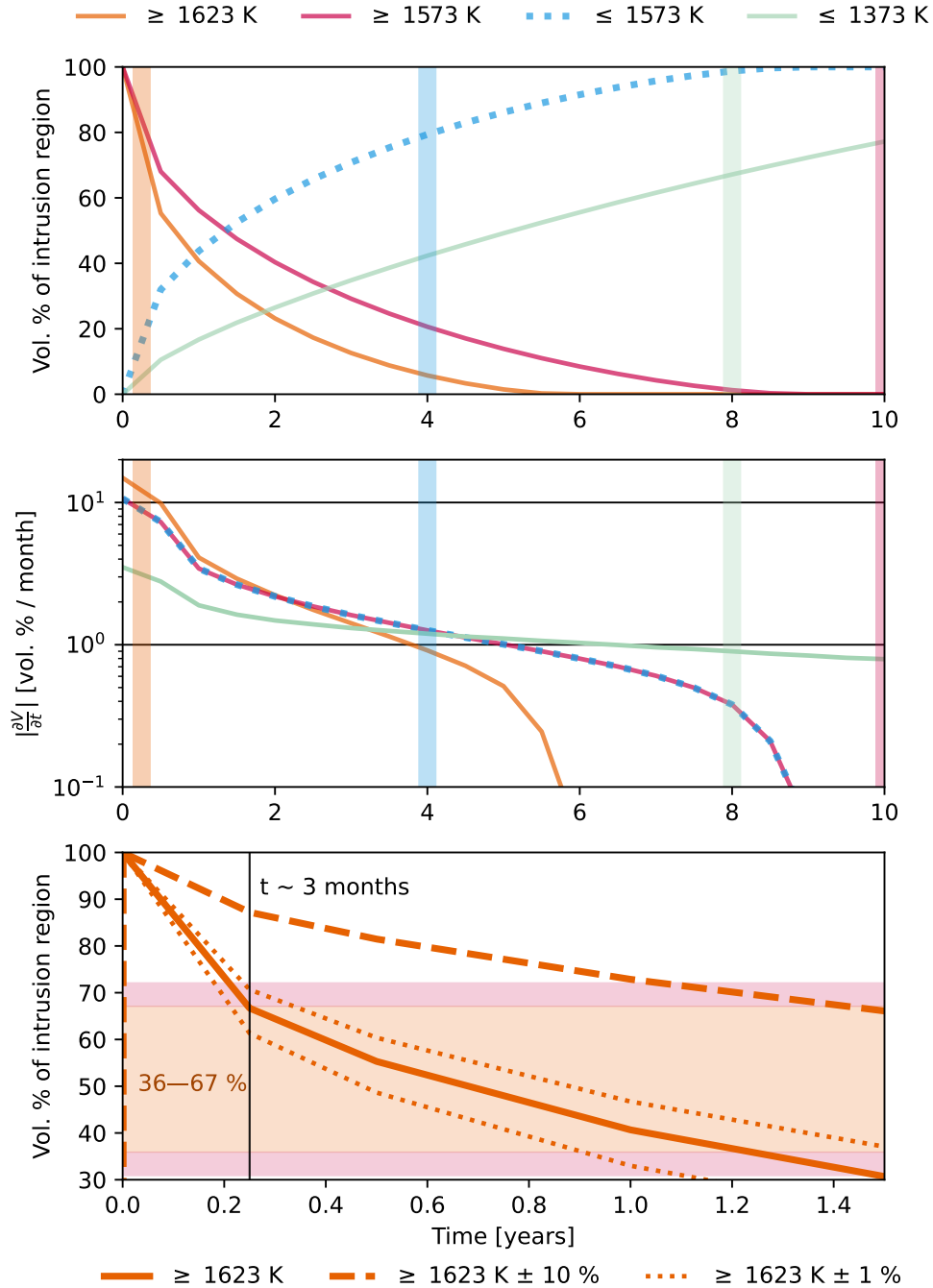


Figure S5: Exploration of the effect of time of measurement for each of the rounding and zoning criteria. The top panel shows the volume % of the region of the intrusion that matches each requirement through time, and the corresponding time that this measurement is taken (matching colour vertical line). The second panel shows the rate of change of intrusion volume that matches each criterion, per month (where the timestep is  $\sim 1$  month). The bottom panel is a zoomed view of the first criteria ( $T_{3\text{months}} \geq 1623$  K), which is the most sensitive to timing. This plot also shows the volume % of the region that matches the criteria if the temperature requirement is varied by  $\pm 10\%$  or  $\pm 1\%$ . The rounding requirement volume is shown in shaded orange, with an additional  $\pm 5\%$  shown in pink.

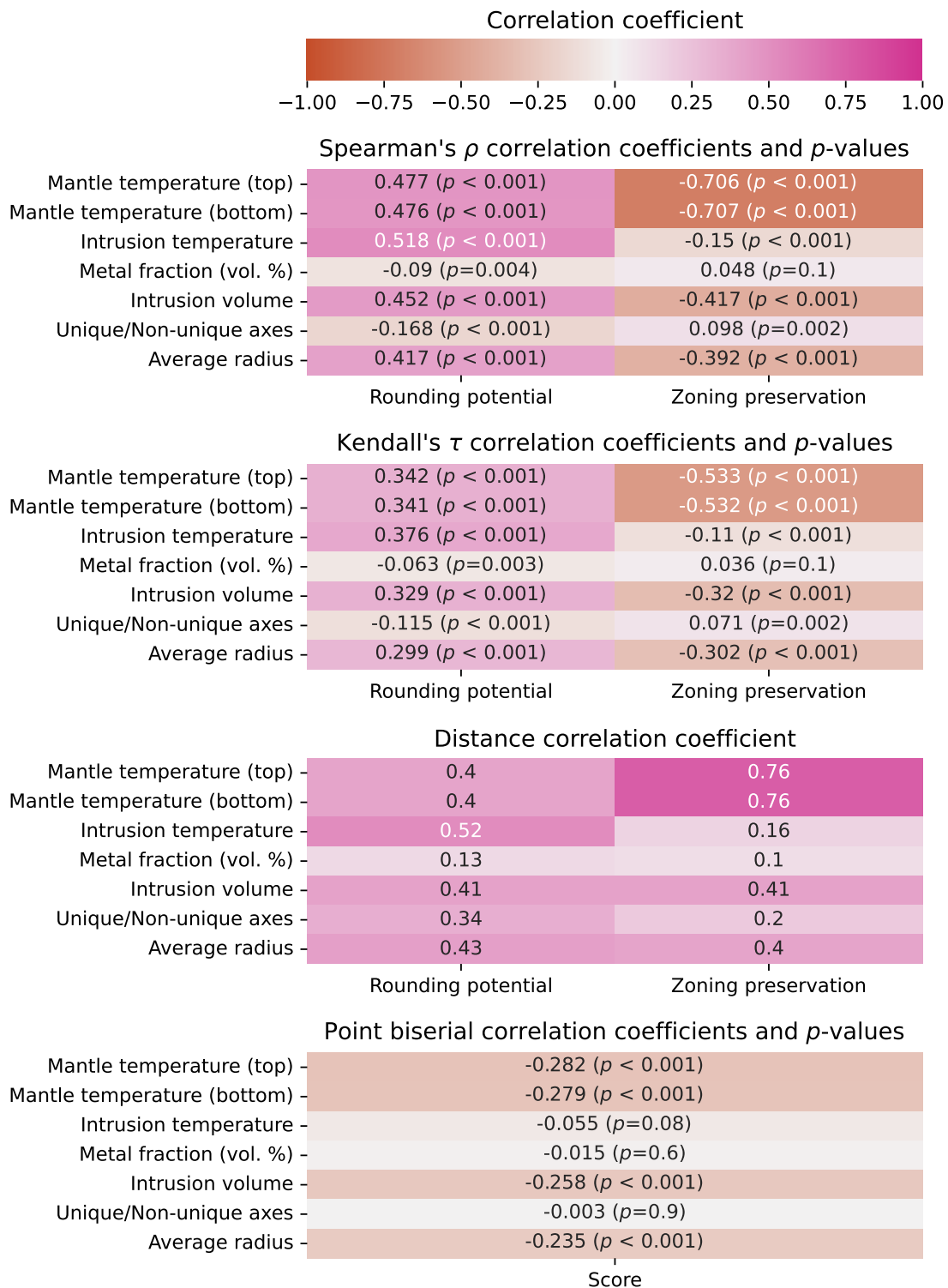


Figure S6: Monotonic and non-monotonic estimations of correlation with  $p$  value where relevant, for a suite of initial conditions and resulting volume % that match the rounding and zoning preservation criteria, as well as the overall score (where score was reduced to a binary pass/fail, with scores of 0 and 1 grouped into the fail category).



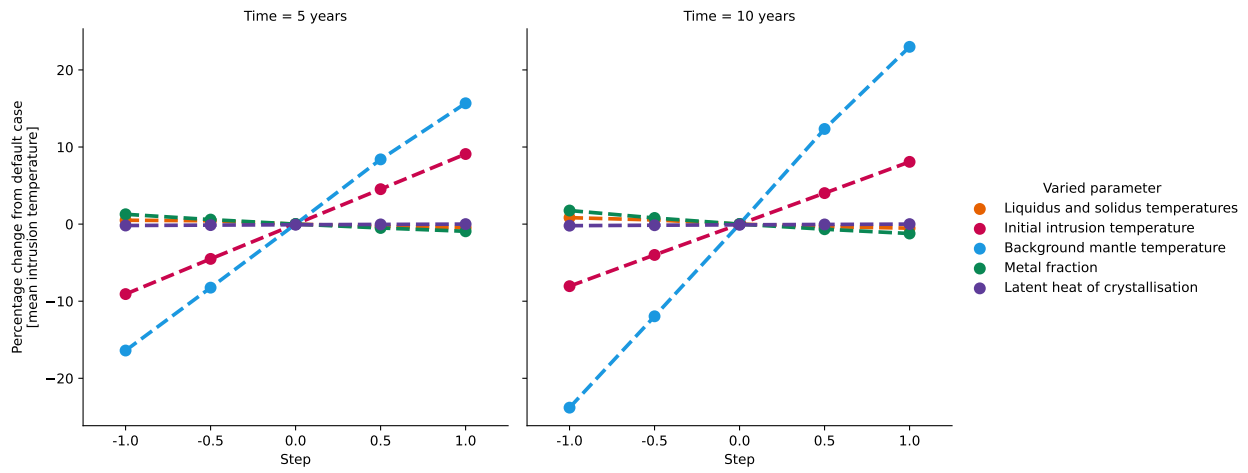


Figure S7: Sensitivity testing; varying parameters individually across a maximum, minimum and mean value. Details given in Table S1.

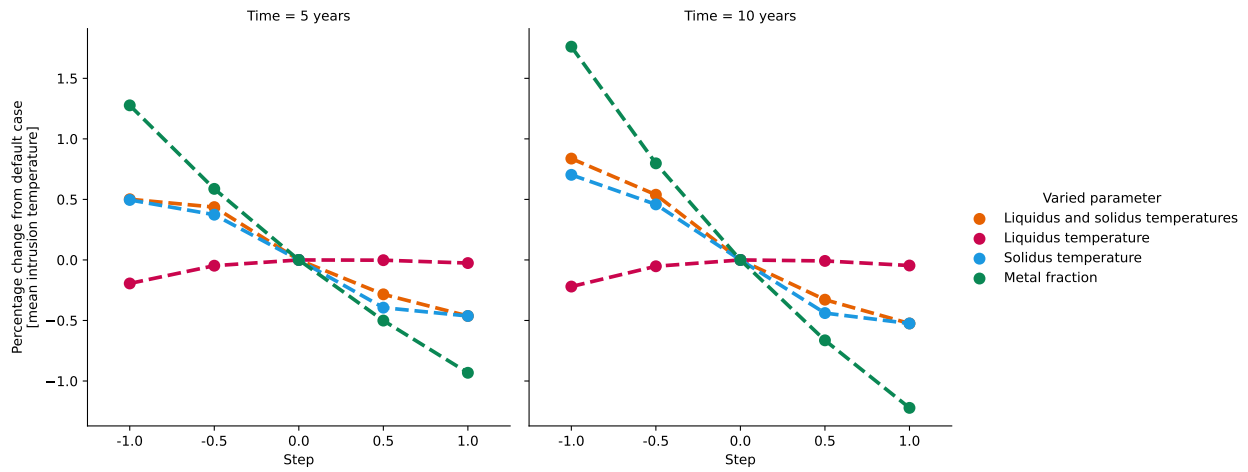


Figure S8: Sensitivity testing; varying parameters individually across a maximum, minimum and mean value, zoom in on less sensitive parameters. Details given in Table S1.

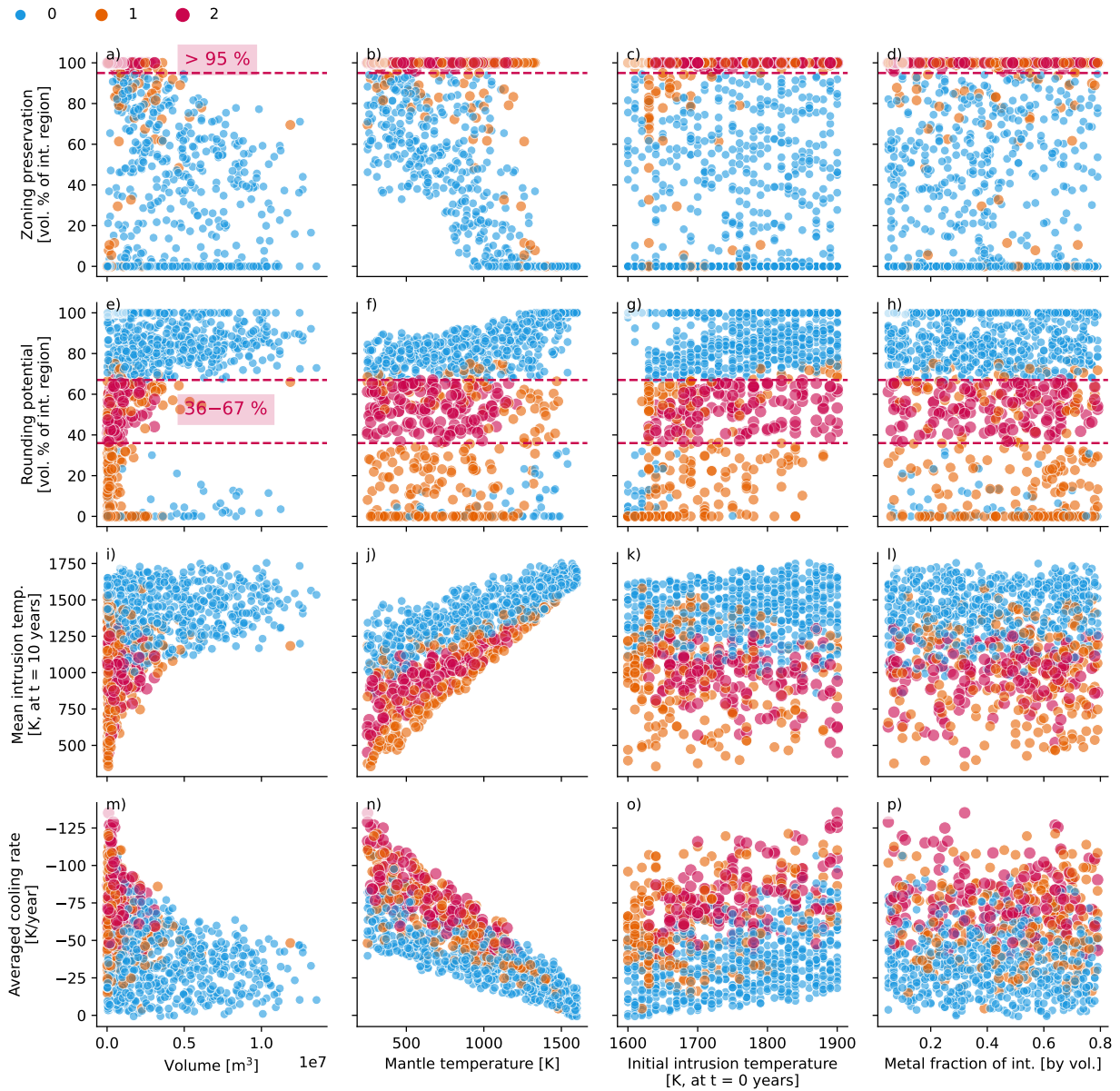


Figure S9: Summary of results for 1000 model runs where material properties were allowed to vary randomly in addition to geometry-related parameters. Colour denotes score: 0 means neither constraint was matched, 1 means one constraint was matched, and 2 means both constraints were matched. Marker shape describes the initial temperature conditions: either output from a planetesimal model, or randomly assigned. Parameters were not varied in isolation. Large pink circles match both constraints and used input from a planetesimal model.

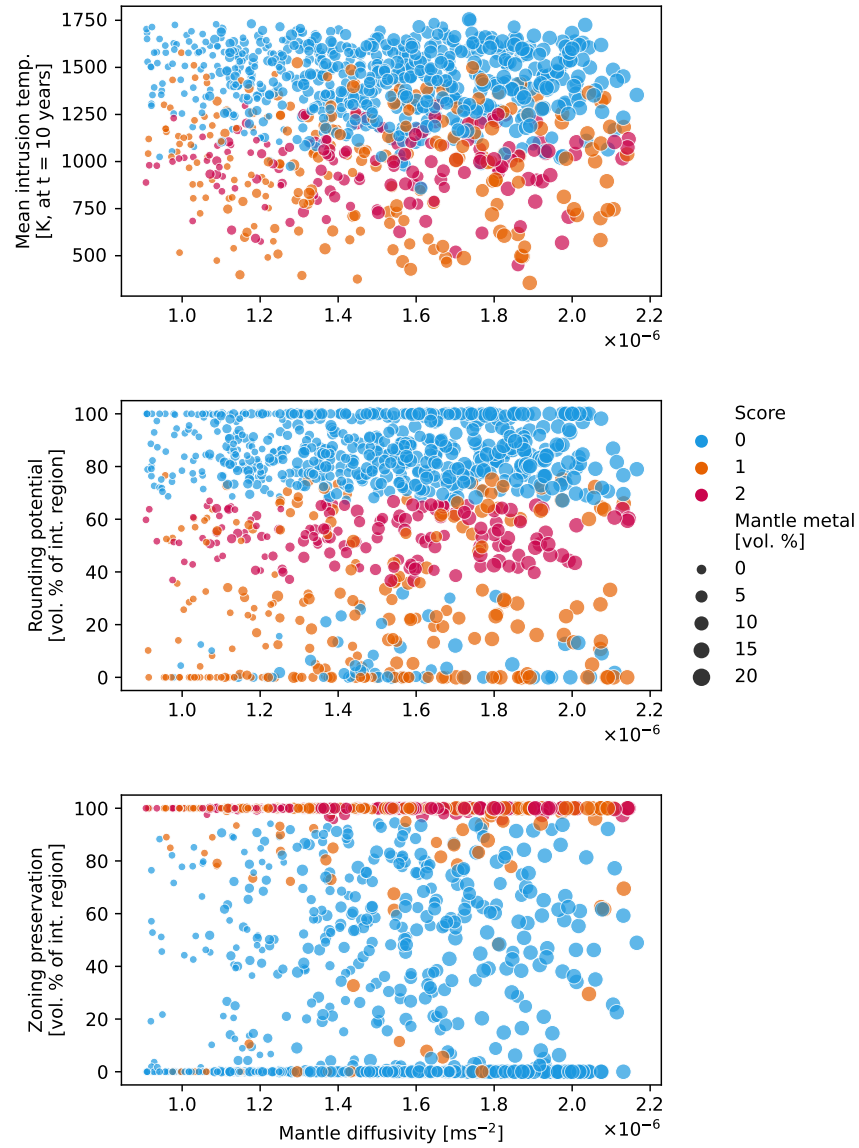


Figure S10: Summary of results for 1000 model runs where material properties were allowed to vary randomly in addition to geometry-related parameters, highlighting the effect of varying the proportion of trapped metal in the mantle and mantle diffusivity. Colour denotes score: 0 means neither constraint was matched, 1 means one constraint was matched, and 2 means both constraints were matched. Marker shape describes the initial temperature conditions: either output from a planetesimal model, or randomly assigned. Parameters were not varied in isolation. Large pink circles match both constraints and used input from a planetesimal model. No significant correlation was found between fraction of metal trapped in the mantle and model score.

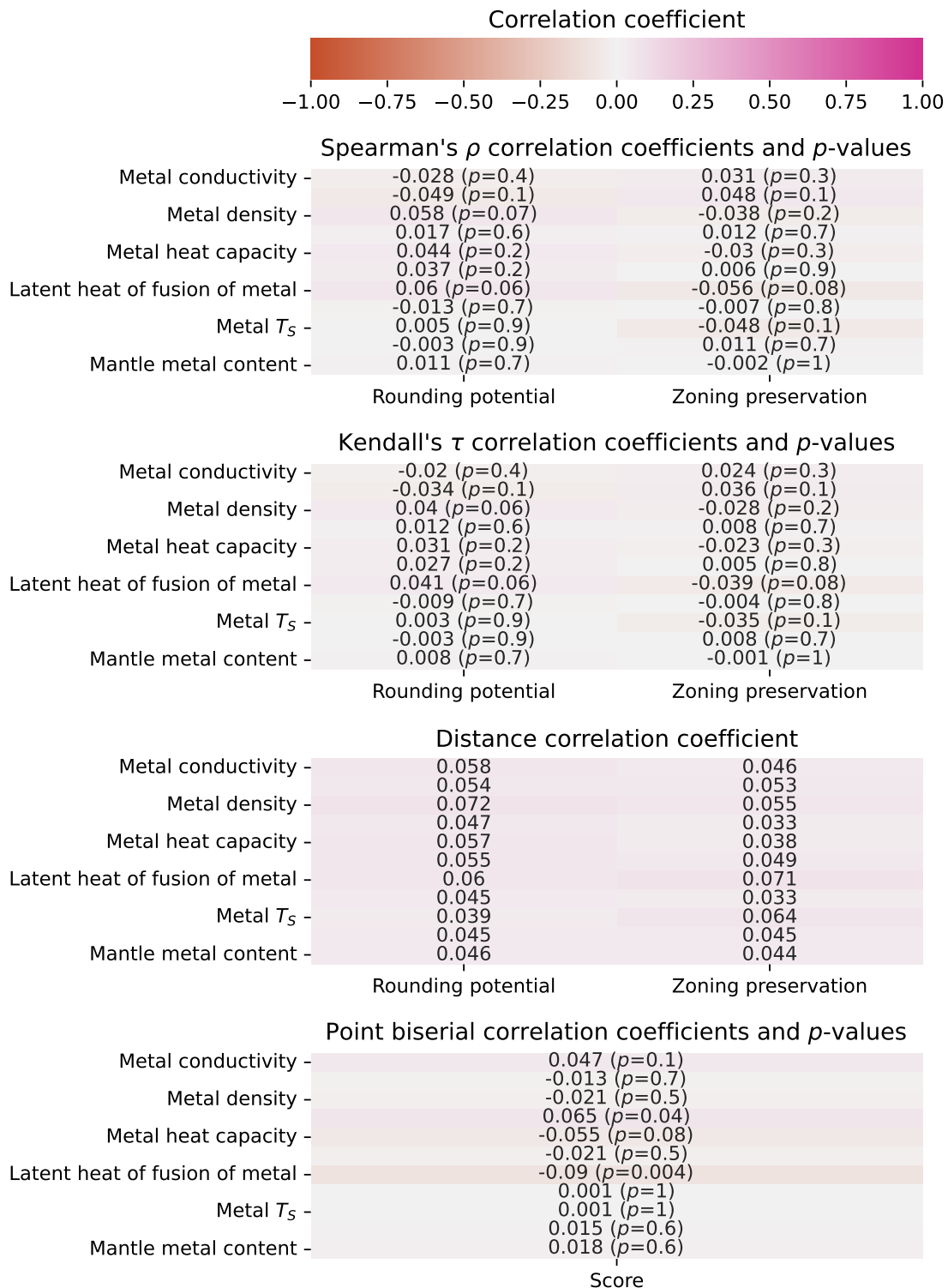


Figure S11: Monotonic and non-monotonic estimations of correlation with  $p$  value where relevant, for a suite of initial conditions (specifically related to material properties) and resulting volume % that match the rounding and zoning preservation criteria, as well as the overall score (where score was reduced to a binary pass/fail, with scores of 0 and 1 grouped into the fail category).

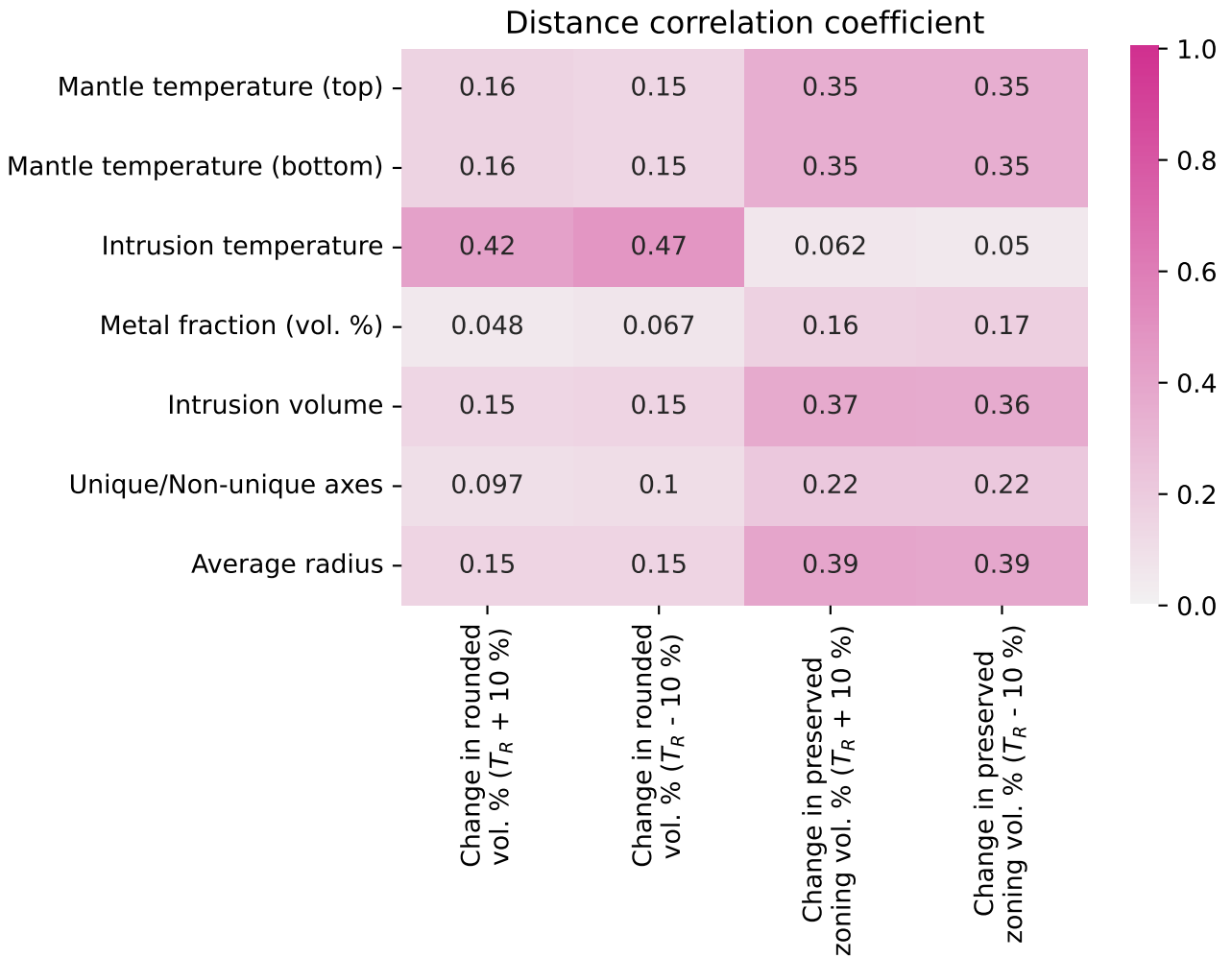


Figure S12: Non-monotonic distance correlation between change in volume % rounded and volume % zoning preserved when the temperature filters are changed by  $\pm 10\%$  of the original temperature, and parameters such as mantle temperature, intrusion temperature, and intrusion geometry.

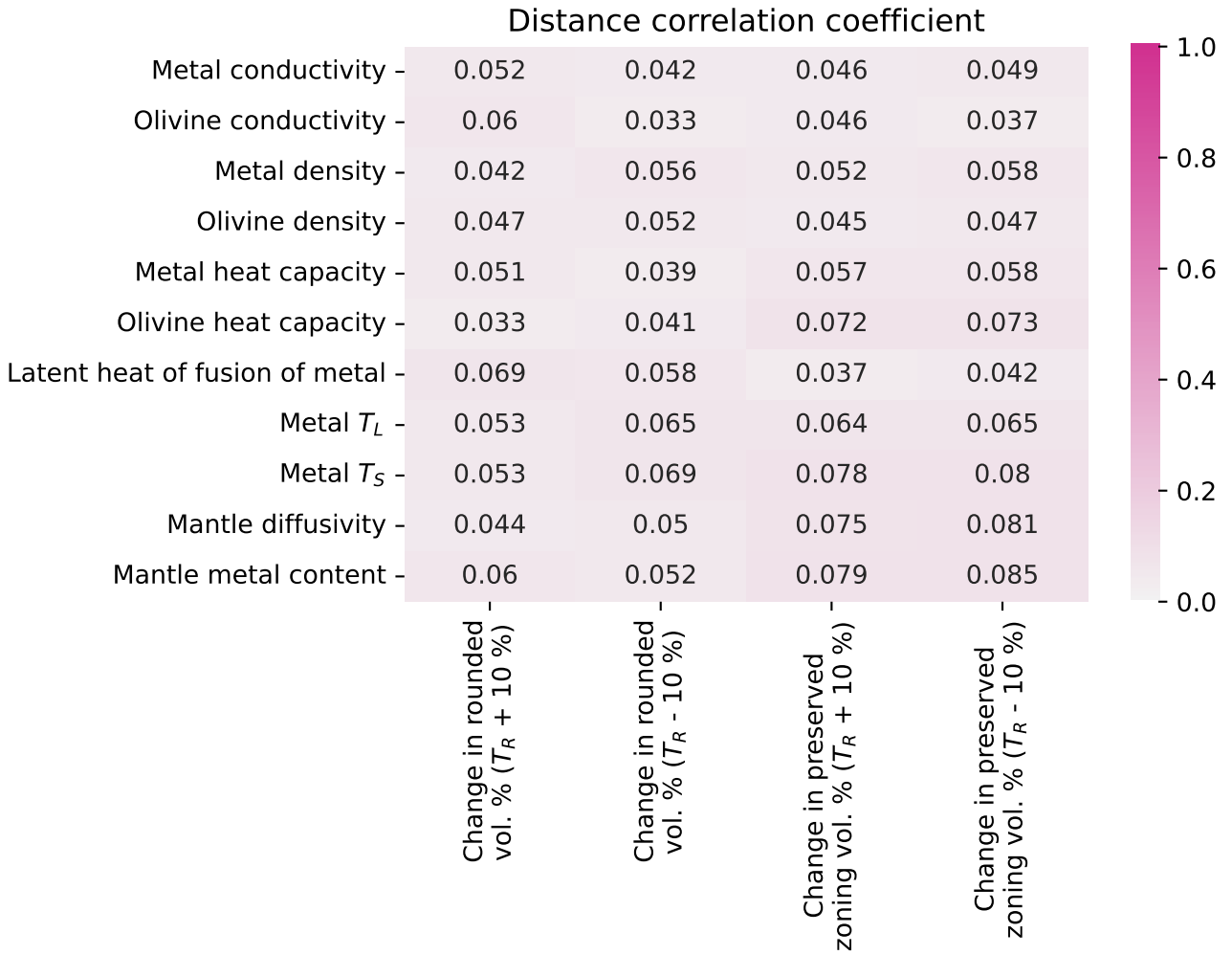


Figure S13: Non-monotonic distance correlation between change in volume % rounded and volume % zoning preserved when the temperature filters are changed by  $\pm 10\%$  of the original temperature, and parameters relating to the material properties of the intrusion region.

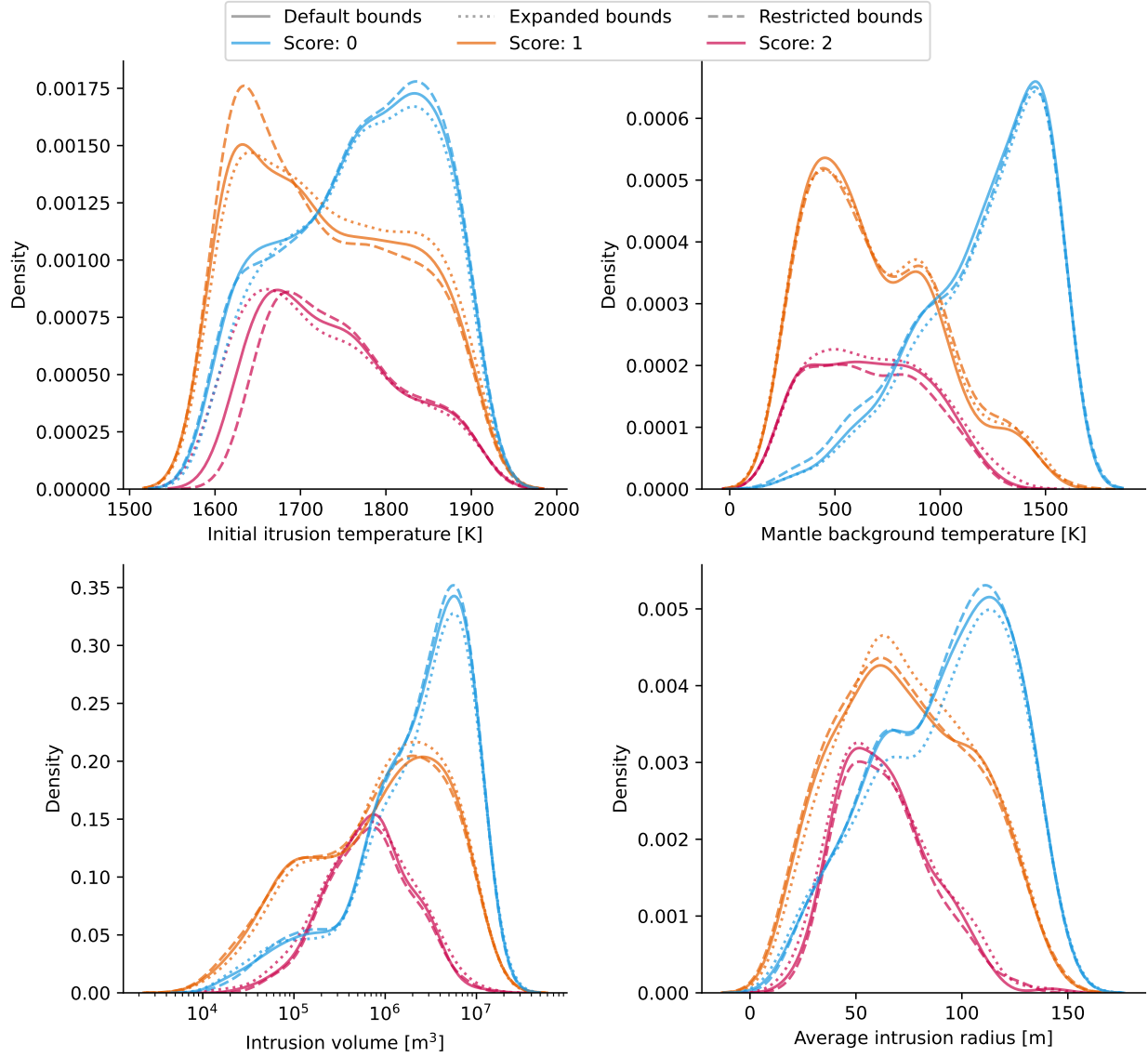


Figure S14: Kernel density estimates for model score vs. initial intrusion temperature, background mantle temperature, intrusion volume (log scale) and average intrusion radius, showing change with “restricted” and “expanded” bounds ( $\pm 10\%$ ). “Restricting” the bounds makes it more difficult for a model to pass the requirements, by increasing the rounding temperature cut-off by  $+10\%$ , and decreasing the zoning temperature cut-off by  $-10\%$ . “Expanding” the bounds is the opposite; by increasing the zoning temperature cut-off by  $+10\%$ , and decreasing the rounding temperature cut-off by  $-10\%$ , resulting in more models with a score of 2.

Table S1: Summary of model runs for sensitivity testing; results shown in Figures S7, S8.  $L_{x,y,z} = 400$  m,  $\Delta x, y, z = 2$  m,  $r_{x,y,z} = 80$  m, material properties of metal and olivine set equal to example case in the main text. Values listed below were set to the mean value (in **bold**) unless they were being varied.

	<b>Step:</b>	<b>-1</b>	<b>-0.5</b>	<b>0</b>	<b>0.5</b>	<b>1</b>
<b>Parameter varied</b>	<b>Unit</b>	Minimum		Mean		Maximum
<b>Liquidus Temperature</b>	K	1570	1630.25	<b>1690.5</b>	1750.75	1811
<b>Solidus Temperature</b>	K	1260	1395	<b>1530</b>	1665	1800
<b>Liquidus and Solidus Temperatures</b>	K					
<b>Initial intrusion temperature</b>	K	1600	1700	<b>1800</b>	1900	2000
<b>Background mantle temperature</b>	K	250	637.5	<b>1025</b>	1412.5	1800
<b>Metal fraction</b>	Volume fraction	0.1	0.2	<b>0.3</b>	0.4	0.5
<b>Latent heat</b>	J/kg	133000	163750	<b>194500</b>	225250	256000



Table S2: Summary of results, with absolute numbers of models receiving each score, and percentage of the model set.

Dataset	Score = 0	Score = 1	Score = 2	Total number	% Score = 0	% Score = 1	% Score = 2
Full dataset	1438	499	263	2200	65.4	22.7	12.0
Planetesimal input	430	124	46	600	71.7	20.7	7.7
r = 250 km	226	51	22	299	75.6	17.1	7.4
r = 300 km	204	73	24	301	67.8	24.3	8.0
Full dataset, with lower req.	1100	757	343	2200	50.0	34.4	15.6
Randomly varied material prop.	626	225	149	1000	62.6	22.5	14.9
Inc. filters by +10 pc	609	246	145	1000	60.9	24.6	14.5
Dec. filters by -10 pc	628	214	158	1000	62.8	21.4	15.8
Expand filters by 10 pc	618	216	166	1000	61.8	21.6	16.6
Restrict filters by 10 pc	619	244	137	1000	61.9	24.4	13.7

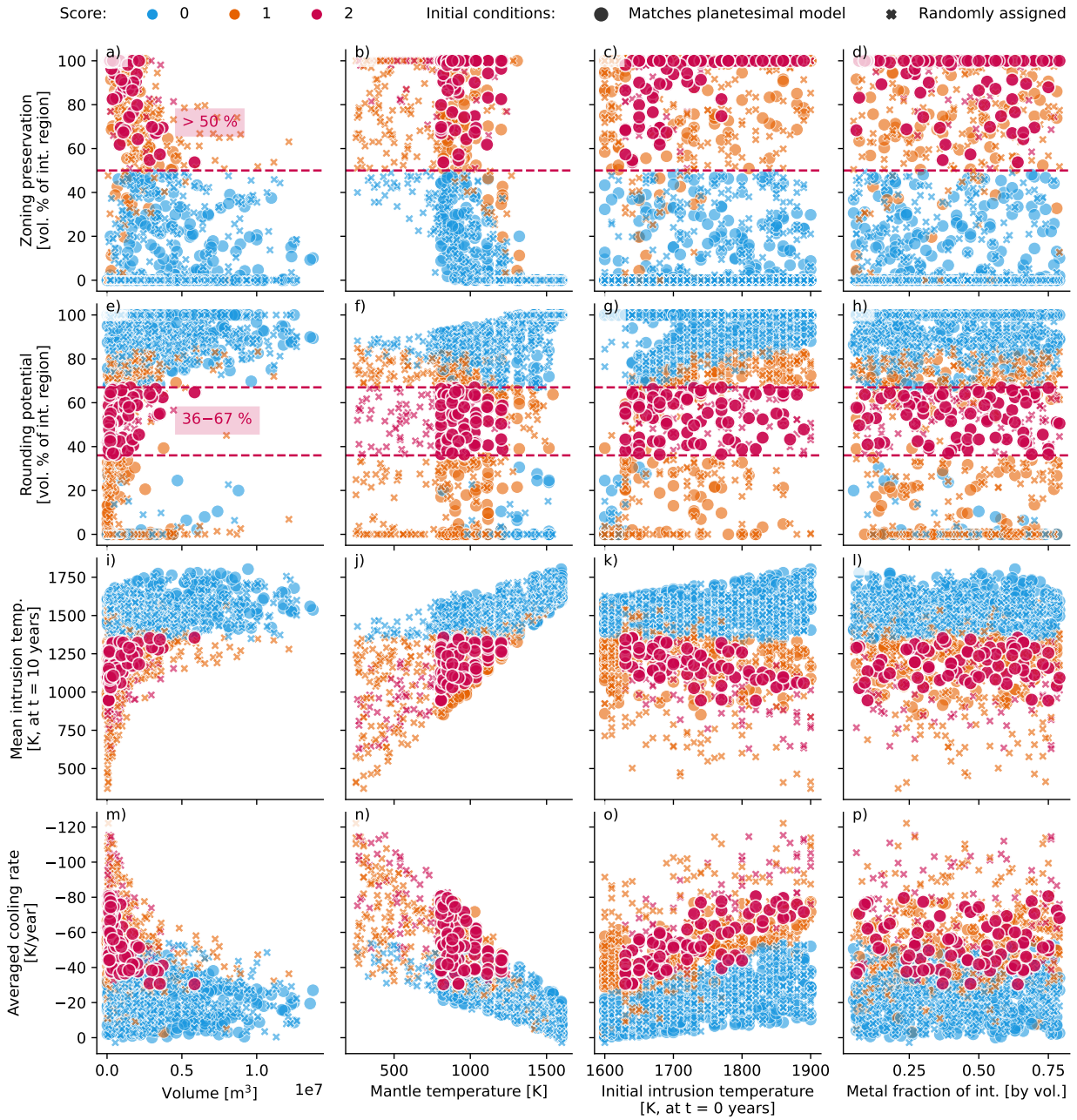


Figure S15: Summary of results for 1200 model runs with a less restrictive zoning criterion  $> 50\%$ , showing that overall trends and conclusions stay the same. Colour denotes score: 0 means neither constraint was matched, 1 means one constraint was matched, and 2 means both constraints were matched. Marker shape describes the initial temperature conditions: either output from a planetesimal model, or randomly assigned. Parameters were not varied in isolation. Large pink circles match both constraints and used input from a planetesimal model.

## References

- 84
- 85 J. S. Boesenberg, J. S. Delaney, and R. H. Hewins. A petrological and chemical reexamination of  
86 main group pallasite formation. *Geochimica et Cosmochimica Acta*, 89:134–158, July 2012. doi:  
87 10.1016/j.gca.2012.04.037. URL <https://doi.org/10.1016/j.gca.2012.04.037>.
- 88 H. S. Carslaw and J. C. Jaeger. *Conduction of heat in solids*. Clarendon Press ; Oxford University Press,  
89 Oxford : New York, 2nd edition, 1959.
- 90 W. Cen, R. Hoppe, and N. Gu. Fast and accurate determination of 3D temperature distribution using  
91 fraction-step semi-implicit method. *AIP Advances*, 6(9):095305, 2016. doi: 10.1063/1.4962665.
- 92 J. Crank and P. Nicolson. A practical method for numerical evaluation of solutions of partial differential  
93 equations of the heat-conduction type. *Mathematical Proceedings of the Cambridge Philosophical Society*,  
94 43(1):50–67, 1947. doi: 10.1017/s0305004100023197.
- 95 H. P. Langtangen and S. Linge. *Finite Difference Computing with PDEs*. Springer International Publishing,  
96 2017. doi: 10.1007/978-3-319-55456-3. URL <https://doi.org/10.1007/978-3-319-55456-3>.
- 97 S. J. McKibbin, L. Pittarello, C. Makarona, C. Hamann, L. Hecht, S. M. Chernozhkin, S. Goderis,  
98 and P. Claeys. Petrogenesis of main group pallasite meteorites based on relationships among texture,  
99 mineralogy, and geochemistry. *Meteoritics & Planetary Science*, 54(11):2814–2844, 2019. doi:  
100 10.1111/maps.13392. URL <https://onlinelibrary.wiley.com/doi/abs/10.1111/maps.13392>.
- 101 D. Mottaghy and V. Rath. Latent heat effects in subsurface heat transport modelling and their impact  
102 on palaeotemperature reconstructions. *Geophysical Journal International*, 164(1):236–245, 2006. doi:  
103 10.1111/j.1365-246x.2005.02843.x.
- 104 M. Özisik. *Heat conduction*. Wiley, New York, 1993.
- 105 R. Roy, A. Beck, and Y. Touloukian. Thermo-Physical Properties of Rocks. *McGraw-Hill CINDAS Data*  
106 *Series on Material Properties*, 11:409–502, 1981.
- 107 S. Sahijpal. Thermal evolution of non-spherical asteroids in the early solar system. *Icarus*, page 114439,  
108 2021. doi: 10.1016/j.icarus.2021.114439.
- 109 I. Sarbu and C. Sebarhievici. Thermal Energy Storage. In *Solar Heating and Cooling Systems:  
110 Fundamentals, Experiments and Applications*, pages 99–138. Elsevier, 2017. doi: 10.1016/b978-0-12-  
111 811662-3.00004-9.

- 112 J. T. Wasson and B.-G. Choi. Main-group pallasites. *Geochimica et Cosmochimica Acta*, 67(16):3079–3096,  
113 2003. doi: 10.1016/s0016-7037(03)00306-5.
- 114 N. N. Yanenko. *The Method of Fractional Steps*. Springer Berlin Heidelberg, 1971. doi: 10.1007/978-3-642-  
115 65108-3.
- 116 M. Zeneli, A. Nikolopoulos, S. Karellas, and N. Nikolopoulos. Numerical methods for solid-liquid phase-  
117 change problems. In *Ultra-High Temperature Thermal Energy Storage, Transfer and Conversion*, pages  
118 165–199. Elsevier, 2021. doi: 10.1016/b978-0-12-819955-8.00007-7.